INTERNATIONAL JOURNAL OF ADAPTIVE CONTROL AND SIGNAL PROCESSING
*Int. J. Adapt. Control Signal Process.* 0000; **00**:1–24
Published online in Wiley InterScience (www.interscience.wiley.com). DOI: 10.1002/acs

# Icing Detection and Identification for Unmanned Aerial Vehicles using Nested Multiple Models

Andrea Cristofaro*, Tor Arne Johansen, A. Pedro Aguiar

*A. Cristofaro is with School of Science and Technology–Mathematics Division, University of Camerino, Italy* andrea.cristofaro@unicam.it.
*T.A. Johansen is with Department of Engineering Cybernetics, Norwegian University of Science and Technology and with Center for Autonomous Marine Operations and Systems (NTNU-AMOS), Trondheim, Norway* tor.arne.johansen@itk.ntnu.no.
*A.P. Aguiar is with Research Center for Systems and Technologies, Faculty of Engineering, University of Porto (FEUP), Porto, Portugal* pedro.aguiar@fe.up.pt.

SUMMARY

A multiple model approach for icing diagnosis and identification in small unmanned aerial vehicles (UAVs) is proposed. The accretion of ice layers on wings and control surfaces modifies the shape of the aircraft and, consequently, alters performance and controllability of the vehicle. Pitot tubes might be blocked due to icing, providing errors in the airspeed measurements. In this paper we propose a nested multiple model adaptive estimation framework to detect and estimate icing using standard sensors only, i.e. a pitot tube and IMU. The architecture of the estimation scheme is based on two different time scales, i.e. one for accretion of ice on aircraft surfaces and one for accretion of ice on sensors, and consists in two nested adaptive observers, namely outer and inner loop respectively. The case-study of a typical small UAV supports and validates the proposed theoretical results. Copyright © 0000 John Wiley & Sons, Ltd.

Received ...

## 1. INTRODUCTION

The efficiency and reliability of operations in isolated areas have significantly increased thanks to the development of advanced control systems and the use of automated vehicles. On the other hand, such systems are expected to face very critical and harsh conditions. Unmanned aerial vehicles (UAVs), whose employment as support to operations in remote environments is becoming more and more crucial, are naturally prone to the occurrence of icing. Detection and accommodation of ice adhesion on wings, control surfaces and sensors is a challenging and primary issue for UAVs, since the ice accretion modifies the shape of the aircraft and alters the measurements, this causing adverse changes on aerodynamic forces and reducing the maneouvring capabilities. In this regard, fault diagnosis and fault tolerant control has been widely investigated in recent years [1] [2], with the aim of designing scheme to recover system performances and preventing hazardous operational conditions.
The phenomenon of icing, that can be regarded as a structural fault, is a well recognized problem in aviation research since the early 1900s [3]. The formation of ice layers decrease the lift and, simultaneously, increase the drag and the mass of the vehicle, this requiring additional engine power and implying a premature stall angle [4]. Inflight icing is typically caused by the

*Corresponding author

impact of supercooled water droplets (SWD). When a water droplet is cooled, it does not freeze until it reaches very low temperatures; however, if the droplet impact on the aircraft surface it may freeze immediately and then accretes ice [5]. The rate and the severity of icing are determined by several factors, such as shape and roughness of the impacting surface, vehicle speed, surface temperature, air temperature and relative humidity [6].
The consequences of icing are even more severe for small unmanned aircrafts due to their simple architecture and limited payload, this making them mostly unsuitable for the typical anti-icing and de-icing devices that are used in large airplanes. Small UAVs are also more prone to icing than most other aircrafts since they often operate at low altitude where high humidity and SWD are encountered more frequently. Larger aircraft tend to operate at high altitude (except for take off and landing) where there are less risks of icing. Some advanced de-icing systems for UAVs have been recently proposed based on carbon nanotube technology [7] [8]. The wing surface can be painted with layers of coating material made of carbon nanotubes, which can be heated up very quickly using an onboard electric energy source. However, since this is very power consuming, in order to guarantee the efficiency of the system it is very important to rely on fault/icing detection schemes with fast and accurate responses. Several approaches have been proposed for icing detection in aircrafts and unmanned aerial vehicles. Actuator fault detection methods have been investigated in [9] [10], while a KF-innovation approach is proposed in [11]. The problem of sensor icing diagnosis is addressed in [12] [13], where residuals based on statistical and comparison methods have been adopted. Detection and isolation schemes using Unknown Input Observers have been proposed for lateral dynamics [14] and, recently, for longitudinal dynamics [15]. In this paper we adopt a multiple-model (MM) approach [16] [17] [18] [19] [20]. Defining a bank of possible models, corresponding to distinct admissible values of the icing severity factor, the proposed algorithm guarantees the identification of the closest model to the true system as well as the estimation of the icing severity factor. The main advantages of the MM framework are cost-efficiency, robustness, parallel structure and fast transient response. The work of icing detection and identification using MM has been initiated with [21, 22] for the longitudinal dynamics. This paper extends previous results in two different directions: the complete 6-DOF aircraft model is considered, and an enhanced MM estimation technique is proposed based on nested algorithms. Specifically, the main contributions of the paper are the rigorous demonstration of adaptive multiple-model convergence in the case of time-varying parameters and the design of two nested blocks of multiple models with the aim of estimating the icing coefficients for the aircraft surface and for the airspeed sensor, these being characterized by different time scales. The paper is structured as follows. The UAV model and the basic setup are given in Section II. while the multiple-model framework is introduced in Section III. The main results are presented in Section IV. Finally, Section V is dedicated to the validation of the proposed results by means of numerical simulations.

**Notation:** Scalar quantities are denoted with roman symbols (lowercase, capital and greek); bold lowercase symbols denote vectors and bold capital symbols denote matrices.

## 2. UAV MODEL

Consider the standard aircraft nonlinear model with quasi-linear aerodynamical forces [23], consisting of three equations for airspeed components $(\tilde{u}, \tilde{v}, \tilde{w})$ representing velocity relative to the wind along the main body axes, three equations for Euler angles $(\tilde{\phi}, \tilde{\theta}, \tilde{\psi})$ defining the




DOI: 10.1002/acs

attitude of the vehicle and three equations for angular rates $(\tilde{p}, \tilde{q}, \tilde{r})$:

$$
\begin{aligned}
\dot{\tilde{u}} &= \tilde{r}\tilde{v} - \tilde{q}\tilde{w} - g\sin\tilde{\theta} + a_x \\
\dot{\tilde{v}} &= \tilde{p}\tilde{w} - \tilde{r}\tilde{u} + g\cos\tilde{\theta}\sin\tilde{\phi} + a_y \\
\dot{\tilde{w}} &= \tilde{q}\tilde{u} - \tilde{p}\tilde{v} + g\cos\tilde{\theta}\cos\tilde{\phi} + a_z \\
\\
\dot{\tilde{\phi}} &= \tilde{p} + \tilde{q}\sin\tilde{\phi}\tan\tilde{\theta} + \tilde{r}\cos\tilde{\phi}\tan\tilde{\theta} \\
\dot{\tilde{\theta}} &= \tilde{q}\cos\tilde{\phi} - \tilde{r}\sin\tilde{\phi} \\
\dot{\tilde{\psi}} &= \tilde{q}\sin\tilde{\phi}\sec\tilde{\theta} + \tilde{r}\cos\tilde{\phi}\sec\tilde{\theta} \\
\\
\dot{\tilde{p}} &= \Gamma_1\tilde{p}\tilde{q} - \Gamma_2\tilde{q}\tilde{r} + \Gamma_3 P + \Gamma_4 R \\
\dot{\tilde{q}} &= \Gamma_5\tilde{p}\tilde{r} - \Gamma_6(\tilde{p}^2 - \tilde{r}^2) + Q/J_y \\
\dot{\tilde{r}} &= \Gamma_7\tilde{p}\tilde{q} - \Gamma_1\tilde{q}\tilde{r} + \Gamma_4 P + \Gamma_8 R
\end{aligned}
\tag{1}
$$

where $g$ is the gravity acceleration and $J_y, \Gamma_i$ are inertia coefficients. Except when specifically indicated, throughout the paper we will refer to quantities expressed in the body-fixed coordinate frame.

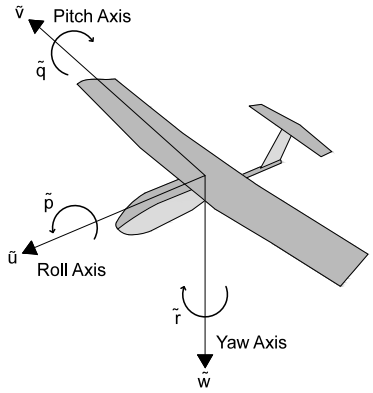


Figure 1. UAV model with body-fixed coordinate frame

The translational accelerations $a_x, a_y, a_z$ and the angular accelerations $P, Q, R$ incorporate the effects of aerodynamical forces such as lift, drag and thrust, and are given by [23, 24]

$$
\begin{aligned}
a_x &= \frac{\rho\tilde{V}_a^2 S}{2m}\left(C_X(\tilde{\alpha}) + C_{X_q}(\tilde{\alpha})\frac{c\tilde{q}}{2\tilde{V}_a} + C_{X_{\delta_e}}(\tilde{\alpha})\tilde{\delta}_e\right) \\
&\quad + \frac{\rho K}{2m}(c_t^2\tilde{\delta}_t^2 - \tilde{V}_a^2) \\
a_y &= \frac{\rho\tilde{V}_a^2 S}{2m}\left(C_{Y_0} + C_{Y_\beta}\beta + C_{Y_p}\frac{b\tilde{p}}{2\tilde{V}_a}\right. \\
&\quad \left. + C_{Y_r}\frac{b\tilde{r}}{2\tilde{V}_a} + C_{Y_{\delta_a}}\tilde{\delta}_a + C_{Y_{\delta_r}}\tilde{\delta}_r\right) \\
a_z &= \frac{\rho\tilde{V}_a^2 S}{2m}\left(C_Z(\tilde{\alpha}) + C_{Z_q}(\tilde{\alpha})\frac{c\tilde{q}}{2\tilde{V}_a} + C_{Z_{\delta_e}}(\tilde{\alpha})\tilde{\delta}_e\right)
\end{aligned}
\tag{2}
$$



*Prepared using* acsauth.cls
DOI: 10.1002/acs

$$
\begin{aligned}
P &= \frac{\rho \tilde{V}_a^2 S b}{2}\left(C_{p_0} + C_{p_\beta}\tilde{\beta} + C_{p_p}\frac{b\tilde{p}}{2\tilde{V}_a}\right.\\
&\quad \left. + C_{p_r}\frac{b\tilde{r}}{2\tilde{V}_a} + C_{p_{\delta_a}}\tilde{\delta}_a + C_{p_{\delta_r}}\tilde{\delta}_r\right)\\
Q &= \frac{\rho \tilde{V}_a^2 S c}{2}\left(C_{m_0} + C_{m_\alpha}\tilde{\alpha} + C_{m_q}\frac{c\tilde{q}}{2\tilde{V}_a} + C_{m_{\delta_e}}\tilde{\delta}_e\right)\\
R &= \frac{\rho \tilde{V}_a^2 S b}{2}\left(C_{r_0} + C_{r_\beta}\tilde{\beta} + C_{r_p}\frac{b\tilde{p}}{2\tilde{V}_a}\right.\\
&\quad \left. + C_{r_r}\frac{b\tilde{r}}{2\tilde{V}_a} + C_{r_{\delta_a}}\tilde{\delta}_a + C_{r_{\delta_r}}\tilde{\delta}_r\right)
\end{aligned}
\tag{3}
$$

where $\tilde{V}_a$ denotes the total airspeed

$$\tilde{V}_a = \sqrt{\tilde{u}^2 + \tilde{v}^2 + \tilde{w}^2},$$

$m$ is vehicle mass, $\rho$ is the air density, $S$ is the wing surface area, $b, c$ are the airfoil span and chord, respectively. The quantities $\tilde{\alpha}$ and $\tilde{\beta}$ are the angle-of-attack (AOA) and the side-slip angle (SSA), which verify

$$\tilde{\alpha} = \arctan\frac{\tilde{w}}{\tilde{u}}, \quad \tilde{\beta} = \arcsin\frac{\tilde{v}}{\tilde{V}_a}.$$

AOA and SSA are very important parameters in the aircraft stability analysis and control synthesis [25]; in particular AOA is the angle between the incoming airflow and the airfoil main chord, while SSA is the angle between the incoming airflow and the longitudinal body axis.

The coefficients $C_\sharp$ are referred to as stability and control derivatives; it can be noticed that coefficients for horizontal and vertical speed depend on the angle-of-attack $\tilde{\alpha}$ according to

$$
\begin{aligned}
&C_X(\tilde{\alpha}) = -(C_{D_0} + C_{D_\alpha}\tilde{\alpha})\cos\tilde{\alpha} + (C_{L_0} + C_{L_\alpha}\tilde{\alpha})\sin\tilde{\alpha}\\
&C_{X_q}(\tilde{\alpha}) = -C_{D_q}\cos\tilde{\alpha} + C_{L_q}\sin\tilde{\alpha}\\
&C_{X_{\delta_e}}(\tilde{\alpha}) = -C_{D_{\delta_e}}\cos\tilde{\alpha} + C_{L_{\delta_e}}\sin\tilde{\alpha}\\
&C_Z(\tilde{\alpha}) = -(C_{D_0} + C_{D_\alpha}\tilde{\alpha})\sin\tilde{\alpha} - (C_{L_0} + C_{L_\alpha}\tilde{\alpha})\cos\tilde{\alpha}\\
&C_{Z_q}(\tilde{\alpha}) = -C_{D_q}\sin\tilde{\alpha} - C_{L_q}\cos\tilde{\alpha}\\
&C_{Z_{\delta_e}}(\tilde{\alpha}) = -C_{D_{\delta_e}}\sin\tilde{\alpha} - C_{L_{\delta_e}}\cos\tilde{\alpha}
\end{aligned}
$$

Finally, the model inputs are the thrust control variable $\tilde{\delta}_t$ (the constant $K$ and $c_t$ are, respectively, an aerodynamical coefficient for the propeller and an efficiency parameter), and the deflection angles associated to elevator, ailerons and rudder: $\tilde{\delta}_e$, $\tilde{\delta}_a$ and $\tilde{\delta}_r$. In a typical aircraft, the elevator is the surface used to control the pitch while the combined use of ailerons and rudder influence roll and yaw angles. It might be useful to define also a compact representation of the aircraft model, and thus we collect all the previous equations in the nonlinear system

$$\dot{\tilde{\mathbf{x}}} = F(\tilde{\mathbf{x}}, \tilde{\boldsymbol{\delta}}), \tag{4}$$

with state $\tilde{\mathbf{x}} = [\tilde{u}\ \tilde{v}\ \tilde{w}\ \tilde{\phi}\ \tilde{\theta}\ \tilde{\psi}\ \tilde{p}\ \tilde{q}\ \tilde{r}]^T$ and control input $\tilde{\boldsymbol{\delta}} = [\tilde{\delta}_t\ \tilde{\delta}_e\ \tilde{\delta}_a\ \tilde{\delta}_r]$.

### *2.1. Linearization*

For estimation purposes, it is worth deriving a suitable linearized model of the aircraft. In particular, the icing accretion framework proposed in Section 3 is mainly based on a coupled longitudinal/lateral linearized vehicle model. To this end, consider a trim condition

$$
\begin{aligned}
&\mathbf{x}^* := [u^*\ v^*\ w^*\ \phi^*\ \theta^*\ \psi^*\ p^*\ q^*\ r^*]^T\\
&\boldsymbol{\delta}^* = [\delta_t^*\ \delta_e^*\ \delta_a^*\ \delta_r^*]^T
\end{aligned}
$$



*Prepared using* acsauth.cls
DOI: 10.1002/acs

and linearize the above system as follows. Set

$$
\begin{array}{l}
u := \tilde{u} - u^*,\ v := \tilde{v} - v^*,\ w := \tilde{w} - w^* \\
\phi := \tilde{\phi} - \phi^*,\ \theta := \tilde{\theta} - \theta^*,\ \psi := \tilde{\psi} - \psi^* \\
p := \tilde{p} - p^*,\ q := \tilde{q} - q^*,\ r := \tilde{r} - r^* \\
\delta_e := \tilde{\delta}_e - \delta_e^*,\ \delta_t := \tilde{\delta}_t - \delta_t^* \\
\alpha := \tilde{\alpha} - \alpha^*,\ \beta := \tilde{\beta} - \beta^*
\end{array}
$$

Incorporating these last expressions, we obtain a 6-DOF linear system describing the linearized coupled longitudinal/lateral dynamics of the aircraft:

$$
\dot{\mathbf{x}} = \mathbf{A}\mathbf{x} + \mathbf{B}\boldsymbol{\delta} \tag{5}
$$

with $\mathbf{x} = [u\ v\ w\ \phi\ \theta\ \psi\ p\ q\ r]^T$, $\boldsymbol{\delta} = [\delta_t\ \delta_e\ \delta_a\ \delta_r]^T$ and

$$
\mathbf{A} = \begin{bmatrix}
X_u & X_v & X_w & 0 & X_\theta & 0 & 0 & X_q & X_r \\
Y_u & Y_v & Y_w & Y_\phi & Y_\theta & 0 & Y_p & 0 & Y_r \\
Z_u & Z_v & Z_w & Z_\phi & Z_\theta & 0 & Z_p & Z_q & 0 \\
0 & 0 & 0 & \Phi_\phi & \Phi_\theta & 0 & \Phi_p & \Phi_q & \Phi_r \\
0 & 0 & 0 & \Theta_\phi & 0 & 0 & 0 & \Theta_q & \Theta_r \\
0 & 0 & 0 & \Psi_\phi & \Psi_\theta & 0 & 0 & \Psi_q & \Psi_r \\
L_u & L_v & L_w & 0 & 0 & 0 & L_p & L_q & L_r \\
M_u & M_v & M_w & 0 & 0 & 0 & M_p & M_q & M_r \\
N_u & N_v & N_w & 0 & 0 & 0 & N_p & N_q & N_r
\end{bmatrix}
$$

$$
\mathbf{B} = \begin{bmatrix}
X_{\delta_t} & X_{\delta_e} & 0 & 0 \\
0 & 0 & Y_{\delta_a} & Y_{\delta_r} \\
0 & Z_{\delta_e} & 0 & 0 \\
0 & 0 & 0 & 0 \\
0 & 0 & 0 & 0 \\
0 & 0 & 0 & 0 \\
0 & 0 & L_{\delta_a} & L_{\delta_r} \\
0 & M_{\delta_e} & 0 & 0 \\
0 & 0 & N_{\delta_a} & N_{\delta_r}
\end{bmatrix}
$$

The expressions of the coefficients appearing in the matrices are reported in Appendix. We point out that the advantage of using the full 6-DOF model is the availability of a unified approach that can handle maneuvers involving the coupled dynamics and can also be readily adapted to decoupled longitudinal and lateral dynamics.

### *2.2. Input disturbances*

The system dynamics is affected by the wind velocity, that can be expressed by the additional input

$$
\begin{bmatrix} \boldsymbol{\mathcal{W}} \\ \mathbf{0}_{6\times 1} \end{bmatrix}, \quad \boldsymbol{\mathcal{W}} = -\mathbf{R}\dot{\tilde{\boldsymbol{\nu}}}
$$

where $\tilde{\boldsymbol{\nu}} = [\tilde{\nu}_N\ \tilde{\nu}_E\ \tilde{\nu}_D]^T$ is the wind speed expressed in the North-East-Down coordinate frame and $\mathbf{R}$ is the rotation matrix

$$
\mathbf{R} = \begin{bmatrix} 1 & 0 & 0 \\ 0 & \cos\phi & \sin\phi \\ 0 & -\sin\phi & \cos\phi \end{bmatrix} \cdot \begin{bmatrix} \cos\theta & 0 & -\sin\theta \\ 0 & 1 & 0 \\ \sin\theta & 0 & \cos\theta \end{bmatrix} \cdot \begin{bmatrix} \cos\psi & \sin\psi & 0 \\ -\sin\psi & \cos\psi & 0 \\ 0 & 0 & 1 \end{bmatrix}
$$



*Prepared using* acsauth.cls
DOI: 10.1002/acs

The wind velocity $\tilde{\boldsymbol{\nu}}$ can be expressed as the sum of a steady component (known or accurately estimated) $\boldsymbol{\nu}^*$ with $\dot{\boldsymbol{\nu}}^* = 0$ and a gust component $\boldsymbol{\nu}$; the linearization yields the linear input disturbance

$$\mathbf{W}\dot{\boldsymbol{\nu}} = \begin{bmatrix} -\mathbf{R}^* \\ \mathbf{0}_{6\times 3} \end{bmatrix} \dot{\boldsymbol{\nu}} \tag{6}$$

where $\mathbf{R}^*$ stands for the matrix $\mathbf{R}$ computed for $\phi = \phi^*, \theta = \theta^*$ and $\psi = \psi^*$.

### *2.3. Measured outputs*

The standard sensor suite for unmanned vehicles includes IMU, compass, GPS and a pitot tube for the airspeed measurement. The measurement of Euler angles $\tilde{\phi}, \tilde{\theta}$ and angular rates $p, q, r$ are provided by the inertial sensors, i.e. gyroscopes and accelerometers, while the pitot tube gives the horizontal airspeed $\tilde{u}$. For the purpose of this paper, we can limit to consider only horizontal airspeed $\tilde{u}$, roll angle $\phi$ and pitch angle $\theta$. The following main system outputs are therefore available:

$$\begin{aligned} \tilde{y}_1 &= \tilde{u} + \mu_u \\ \tilde{y}_2 &= \tilde{\phi} + \mu_\phi \\ \tilde{y}_3 &= \tilde{\theta} + \mu_\theta \end{aligned} \tag{7}$$

where $\mu$ denotes a noise term. Linearization about the trim condition $\mathbf{x}^*$ yields:

$$\mathbf{y} = \mathbf{C}\mathbf{x} + \hat{\boldsymbol{\mu}}$$

with

$$\mathbf{C} = \begin{bmatrix} 1 & 0 & 0 & 0 & 0 & 0 & 0 & 0 & 0 \\ 0 & 0 & 0 & 1 & 0 & 0 & 0 & 0 & 0 \\ 0 & 0 & 0 & 0 & 1 & 0 & 0 & 0 & 0 \end{bmatrix}, \quad \hat{\boldsymbol{\mu}} = \begin{bmatrix} \mu_u \\ \mu_\phi \\ \mu_\theta \end{bmatrix} \tag{8}$$

The noise term $\hat{\boldsymbol{\mu}}$ is assumed to be bounded by a known parameter $\varrho_\mu$, i.e.

$$\|\hat{\boldsymbol{\mu}}\| \leq \varrho_\mu.$$

According to the standard sensors suite mounted on the aircraft, additional outputs are available, such as altitude, ground position and linear accelerations. For the scopes of this paper, it is sufficient to consider the outputs given in (7), although the additional outputs could be used for sensor fault diagnosis. Propeller angular speed and control surfaces position are supposed to be available, as well as a measurement of the total mass of the vehicle (take-off weight minus used fuel). Finally, the aircraft is supposed to be equipped with an air data sensor providing air temperature and humidity, which can be used to predict when icing is more likely to occur based on atmospheric conditions.

## 3. ICING EFFECT MODEL

The accretion of clear ice on the aircraft surfaces modifies stability and control derivatives according to the following linear model [26]

$$C_\sharp^{ice} = (1 + \eta\mathcal{K}_\sharp)C_\sharp, \quad \sharp = X, X_q, X_{\delta_e}, \ldots, r_{\delta_a}, r_{\delta_r}. \tag{9}$$

where $\eta$ is the icing severity factor and the coefficient $\mathcal{K}_\sharp$ depends on aircraft specifications [27]; the clean condition corresponds to $\eta = 0$, while the all iced condition occurs for $\eta = \eta_{\max}$ [4]. It is worth noticing that the coefficients $K_\sharp$ turn out to be negative, so that model (9) corresponds to downscaling of control and stability derivatives.
As a consequence, the effect of icing can be modeled as a perturbation term $\eta\mathbf{F}_{ice}(\tilde{\mathbf{x}}, \tilde{\boldsymbol{\delta}})$, where $\eta$ is a scalar quantity and the vector field $\mathbf{F}_{ice}(\cdot,\cdot)$ includes the variations of acceleration coefficients (2) and moments (3) according to (9). Referring to the linearized model (5),



*Prepared using* acsauth.cls
DOI: 10.1002/acs

the overall effect of icing can be regarded as the additive input $\eta(\mathbf{A}_{\mathcal{E}}\mathbf{x}+\mathbf{B}_{\mathcal{E}}\boldsymbol{\delta}+\bar{\mathbf{F}})$ with $\bar{\mathbf{F}}=\mathbf{F}_{\mathbf{ice}}(\mathbf{x}^*,\boldsymbol{\delta}^*)$ and

$$\mathbf{A}_{\mathcal{E}}=\begin{bmatrix} \mathcal{E}_{X_u} & \mathcal{E}_{X_v} & \mathcal{E}_{X_w} & 0 & 0 & 0 & 0 & \mathcal{E}_{X_q} & 0 \\ \mathcal{E}_{Y_u} & \mathcal{E}_{Y_v} & \mathcal{E}_{Y_w} & 0 & 0 & 0 & \mathcal{E}_{Y_p} & 0 & \mathcal{E}_{Y_r} \\ \mathcal{E}_{Z_u} & \mathcal{E}_{Z_v} & \mathcal{E}_{Z_w} & 0 & 0 & 0 & 0 & \mathcal{E}_{Z_q} & 0 \\ 0 & 0 & 0 & 0 & 0 & 0 & 0 & 0 & 0 \\ 0 & 0 & 0 & 0 & 0 & 0 & 0 & 0 & 0 \\ 0 & 0 & 0 & 0 & 0 & 0 & 0 & 0 & 0 \\ \mathcal{E}_{L_u} & \mathcal{E}_{L_v} & \mathcal{E}_{L_w} & 0 & 0 & 0 & \mathcal{E}_{L_p} & 0 & \mathcal{E}_{L_r} \\ \mathcal{E}_{M_u} & \mathcal{E}_{M_v} & \mathcal{E}_{M_w} & 0 & 0 & 0 & 0 & \mathcal{E}_{M_q} & 0 \\ \mathcal{E}_{N_u} & \mathcal{E}_{N_v} & \mathcal{E}_{N_w} & 0 & 0 & 0 & \mathcal{E}_{N_p} & 0 & \mathcal{E}_{N_r} \end{bmatrix}$$

$$\mathbf{B}_{\mathcal{E}}=\begin{bmatrix} 0 & \mathcal{E}_{X_{\delta_e}} & 0 & 0 \\ 0 & 0 & \mathcal{E}_{Y_{\delta_a}} & \mathcal{E}_{Y_{\delta_r}} \\ 0 & \mathcal{E}_{Z_{\delta_e}} & 0 & 0 \\ 0 & 0 & 0 & 0 \\ 0 & 0 & 0 & 0 \\ 0 & 0 & 0 & 0 \\ 0 & 0 & \mathcal{E}_{L_{\delta_a}} & \mathcal{E}_{L_{\delta_r}} \\ 0 & \mathcal{E}_{M_{\delta_e}} & 0 & 0 \\ 0 & 0 & \mathcal{E}_{N_{\delta_a}} & \mathcal{E}_{N_{\delta_r}} \end{bmatrix}$$

where the coefficients $\mathcal{E}_\sharp$ are obtained from $\mathcal{K}_\sharp$ and $C_\sharp$ by performing linear combinations. The matrices $\mathbf{A}_{\mathcal{E}},\mathbf{B}_{\mathcal{E}}$ model the changes on state and input matrices due to icing, while the constant vector $\bar{\mathbf{F}}$ represent a shift of the equilibrium condition. The icing severity factor evolves according to the law

$$\eta=f(\omega)\chi$$

where $\omega$ is the fraction of water freezing at a point on a surface to the water impinging on the surface,

$$\omega=\frac{\text{mass of water freezing}}{\text{mass of water impinging}},$$

and $\chi$ is the accumulation parameter defined as the mass flux [28]

$$\dot{\chi}=\frac{\wp\lambda V_a}{\varrho c}(1-\iota_{airfoil}), \tag{10}$$

$\wp$ being the collection efficiency, $\lambda$ the liquid water content, $V_a$ is the airspeed, $\varrho$ the ice density, $c$ is the airfoil chord and $\iota_{airfoil}\in[0,1]$ is the airfoil icing protection coefficient. Both the fraction $\omega$ and the ice density $\rho$ depend on the air temperature and the relative humidity. In particular, when the temperature is below $-10°C$ the factor $\omega$ satisfies $\omega\approx 1$, this corresponding to rime ice formation; on the other hand, if the temperature is between $-10°C$ and $0°C$, glaze ice typically appears with $\omega<1$. It has been observed experimentally that the icing severity factor achieves its maximum $\eta_{\max}$ when the freezing fraction $\omega$ is close to the value $\omega_g=0.2$, while it decreases to a steady value as $\omega$ approaches 1 [26]. We consider therefore a piecewise linear behavior of the function $f(\omega)$:

$$f(\omega):=\begin{cases} \dfrac{f_{\max}}{\omega_g}\omega & \omega\in[0,\omega_g] \\ -\left(\dfrac{f_{\max}}{\omega_g(1-\omega_g)}+\dfrac{f_{\text{steady}}}{1-\omega_g}\right)\omega & \\ \quad+\dfrac{f_{\max}}{\omega_g(1-\omega_g)}+\dfrac{(2-\omega_g)f_{\text{steady}}}{1-\omega_g} & \omega\in[\omega_g,1] \end{cases}$$



DOI: 10.1002/acs

with $f_{\max} > f_{\text{steady}} > 0$.
It is worth noting that icing may likely alter also the airspeed measurements, as the pitot tube may be clogged by the ice: this usually results in the over-estimation of the airspeed caused by the increased pressure. Adopting a normalization parameter $\sigma_u$, depending on the sensor specifications, and denoting by $\xi$ the sensor icing severity factor, the effect can be modeled as

$$y_1 = (1 + \sigma_u \xi)u + \xi \sigma_u u^*,$$

that yields

$$\mathbf{y} = (\mathbf{C} + \xi \mathbf{C}_{\mathcal{S}})\mathbf{x} + \xi \bar{\mathbf{u}} + \hat{\boldsymbol{\mu}}$$

where

$$\mathbf{C}_{\mathcal{S}} := \begin{bmatrix} \sigma_u & 0 & 0 & 0 & 0 & 0 & 0 & 0 & 0 \\ 0 & 0 & 0 & 0 & 0 & 0 & 0 & 0 & 0 \\ 0 & 0 & 0 & 0 & 0 & 0 & 0 & 0 & 0 \end{bmatrix}, \ \bar{\mathbf{u}} := \begin{bmatrix} \sigma_u u^* \\ 0 \\ 0 \end{bmatrix}.$$

Similarly to the previous case, the sensor icing severity factor can be expressed as

$$\xi = f(\omega) \cdot \kappa$$

with

$$\dot{\kappa} = \frac{\wp \lambda V_a}{\varrho d}(1 - \iota_{sensor}), \tag{11}$$

where $d$ is the diameter of the pitot tube and $\iota_{sensor}$ is the sensor icing protection coefficient. It should be noticed that $c >> d$: as a matter of fact, sensor icing is typically quicker and possibly more severe; on the other hand, some UAV are equipped with a heated pitot tube, this resulting in $\iota_{sensor} = 1$, and sensor fault accommodation is relatively straightforward. Summarizing, one has the following perturbed plant:

$$\begin{aligned} \dot{\mathbf{x}} &= (\mathbf{A} + \eta \mathbf{A}_{\mathcal{E}})\mathbf{x} + (\mathbf{B} + \eta \mathbf{B}_{\mathcal{E}})\boldsymbol{\delta} + \eta \bar{\mathbf{F}} + \mathbf{W}\dot{\boldsymbol{\nu}} \\ \mathbf{y} &= (\mathbf{C} + \xi \mathbf{C}_{\mathcal{S}})\mathbf{x} + \xi \bar{\mathbf{u}} + \hat{\boldsymbol{\mu}} \end{aligned}$$

## 4. A MULTIPLE-MODEL ADAPTIVE ESTIMATOR

In this section we provide the general architecture of a multiple model adaptive estimator for systems with time-varying unknown parameters that will be specified to the case of the aircraft system with icing in the next section.
Consider a generic LTI discrete-time plant of the form

$$\begin{aligned} \mathbf{x}_{t+1} &= \mathbf{A}_\vartheta \mathbf{x}_t + \mathbf{B}_\vartheta \mathbf{u}_t + \mathbf{W}_\vartheta \boldsymbol{d}_t \\ \mathbf{y}_t &= \mathbf{C}_\vartheta \mathbf{x}_t + \boldsymbol{\mu}_t \end{aligned}$$

where $\mathbf{x}_t \in \mathbb{R}^n$ denotes the state of the system, $\mathbf{u}_t \in \mathbb{R}^m$ is the control input, $\mathbf{y}_t \in \mathbb{R}^p$ is the output and $\boldsymbol{d}_t \in \mathbb{R}^r, \boldsymbol{\mu}_t \in \mathbb{R}^p$ are, respectively, bounded input and output noise terms. The system matrices $\mathbf{A}_\vartheta, \mathbf{B}_\vartheta, \mathbf{C}_\vartheta, \mathbf{W}_\vartheta$ contain unknown constant parameters denoted by the vector $\vartheta$.
Consider a finite set of candidate parameter values $\mathcal{T} := \{\vartheta_1, \vartheta_2, ..., \vartheta_{i_{max}}\}$; a multiple-model adaptive estimator (MMAE) can be designed according to

$$\hat{\mathbf{x}}_t = \sum_{i=1}^{i_{max}} p_t^i \hat{\mathbf{x}}_{t|\vartheta_i} \tag{12}$$

$$\hat{\mathbf{y}}_t = \sum_{i=1}^{i_{max}} p_t^i \hat{\mathbf{y}}_{t|\vartheta_i} \tag{13}$$

$$\hat{\vartheta}_t = \vartheta_{i^\diamond}, \quad i^\diamond := \arg \max_{i \in \{1,...,i_{max}\}} p_t^i \tag{14}$$




DOI: 10.1002/acs

where $\hat{\mathbf{x}}_t, \hat{\mathbf{y}}_t$ and $\hat{\vartheta}_t$ are the estimates of the state, the output and the parameter vector at time $t$ and $p_t^i$ are dynamic weights to be defined. Each estimated state $\hat{\mathbf{x}}_{t|\vartheta_i}$ corresponds to the $i^{th}$ Krener minimax observer [29]

$$\begin{aligned}\hat{\mathbf{x}}_{t+1|\vartheta_i} &= \mathbf{A}_{\vartheta_i}\hat{\mathbf{x}}_{t|\vartheta_i} + \mathbf{B}_{\vartheta_i}\mathbf{u}_t + \mathbf{D}_{\vartheta_i}(\mathbf{y}_t - \mathbf{C}_{\vartheta_i}\hat{\mathbf{x}}_{t|\vartheta_i}) \\ \hat{\mathbf{y}}_{t|\vartheta_i} &= \mathbf{C}_{\vartheta_i}\hat{\mathbf{x}}_{t|\vartheta_i} \\ \mathbf{D}_{\vartheta_i} &= \mathbf{A}_{\vartheta_i}\boldsymbol{\Sigma}_{\vartheta_i}\mathbf{C}_{\vartheta_i}^T[\mathbf{C}_{\vartheta_i}\boldsymbol{\Sigma}_{\vartheta_i}\mathbf{C}_{\vartheta_i}^T + \boldsymbol{\Omega}]^{-1},\end{aligned}$$

with $\boldsymbol{\Sigma}_{\vartheta_i}$ assigned by the discrete algebraic Riccati equation

$$\begin{gathered}-\boldsymbol{\Sigma}_{\vartheta_i} + \mathbf{A}_{\vartheta_i}^T\boldsymbol{\Sigma}_{\vartheta_i}\mathbf{A}_{\vartheta_i} + \mathbf{W}_{\vartheta_i}\boldsymbol{\Xi}\mathbf{W}_{\vartheta_i}^T \\ -\mathbf{A}_{\vartheta_i}^T\boldsymbol{\Sigma}_{\vartheta_i}\mathbf{C}_{\vartheta_i}^T[\mathbf{C}_{\vartheta_i}\boldsymbol{\Sigma}_{\vartheta_i}\mathbf{C}_{\vartheta_i}^T + \boldsymbol{\Omega}]^{-1}\mathbf{C}_{\vartheta_i}\boldsymbol{\Sigma}_{\vartheta_i}\mathbf{A}_{\vartheta_i} = 0,\end{gathered}$$

where $\boldsymbol{\Xi}$ and $\boldsymbol{\Omega}$ are symmetric positive definite matrices, and the pairs $(\mathbf{A}_{\vartheta_i}, \mathbf{W}_{\vartheta_i})$ and $(\mathbf{A}_{\vartheta_i}, \mathbf{C}_{\vartheta_i})$ are controllable and observable, respectively. Solving algebraic Riccati equations is a non trivial problem that goes far beyond the scope of the present paper; the interested reader might refer to [30] for an interesting and extensive survey on available methods. The dynamic weights $p_t^i$ are generated by the recursion

$$p_{t+1}^i = \frac{\gamma_i e^{-s_t^i}}{\sum_{j=1}^{i_{max}} p_t^j \gamma_j e^{-s_t^j}} p_t^i, \tag{15}$$

where $\gamma_i$ is a positive constant coefficient and $s_t^i$ is continuous function called error measuring function, mapping measurable plant signals to nonnegative values. These quantities can be defined as follows:

$$\gamma_i = \frac{1}{\sqrt{||\mathbf{S}_{\vartheta_i}||}}, \quad s_t^i = \frac{1}{2}||\mathbf{y}_t - \hat{\mathbf{y}}_{t|\vartheta_i}||^2_{\mathbf{S}_{\vartheta_i}^{-1}}$$

with $||\mathbf{x}||_{\mathbf{Q}} = (\mathbf{x}^T\mathbf{Q}\mathbf{x})^{1/2}$ and where the positive definite matrix $\mathbf{S}_{\vartheta_i}$ is given by

$$\mathbf{S}_{\vartheta_i} = \mathbf{C}_{\vartheta_i}\boldsymbol{\Sigma}_{\vartheta_i}\mathbf{C}_{\vartheta_i}^T + \boldsymbol{\Omega}.$$

The dynamic weights are defined in order to be positive and to constitute a partition of unity for any $t \geq 0$.

*Definition 4.1*
An admissible weight initial condition (AWIC) is any vector $\boldsymbol{\pi} \in (0,1)^{i_{max}}$ such that

$$\boldsymbol{\pi} = (\pi_1, ..., \pi_{i_{max}}), \quad \sum_{i=1}^{i_{max}} \pi_i = 1$$

The set of all possible AWIC is denoted with $\mathcal{P}$.

*Proposition 4.1*
*Suppose the initial condition is* $\boldsymbol{\pi}_0 = (p_0^1, ..., p_0^{i_{max}}) \in \mathcal{P}$. *Then each* $p_t^i$ *is contained in the interval* $[0,1]$ $\forall t \geq 0$. *Furthermore*

$$\sum_{i=1}^{N} p_t^i = 1 \quad \forall t \geq 0.$$

Moreover, if a distinguishability condition is met, the dynamic weights satisfy a helpful convergence property [19, 31, 32].

*Lemma 4.1*
*Let* $i^\star \in \{1, 2, ..., i_{max}\}$ *be an index of a parameter vector in* $\mathcal{T}$ *and set* $\mathcal{I} := \{1, 2, ...., i_{max}\} \setminus i^\star$. *Suppose that there exist positive constants* $n_1, t_1, \epsilon$ *and* $\epsilon_1$ *such that for all* $t \geq t_1$ *and* $n \geq n_1$




DOI: 10.1002/acs

*the following conditions hold:*

$$\frac{1}{n}\sum_{\tau=t}^{t+n-1}(s_\tau^{i^\star}+\epsilon) < \frac{1}{n}\sum_{\tau=t}^{t+n-1}\min_{j\in\mathcal{I}} s_\tau^j, \tag{16}$$

$$\log\max_{j\in\mathcal{I}}\gamma_j - \log\gamma_{i^\star} < \epsilon_1, \quad \textit{with } \epsilon_1 < \epsilon. \tag{17}$$

*Then the dynamic weights $p_t^i$ satisfy*

$$\lim_{t\to\infty} p_t^{i^\star} = 1, \quad \lim_{t\to\infty} p_t^j = 0 \quad \forall j \in \mathcal{I}.$$

The proofs of Proposition 4.1 and Lemma 4.1 can be found in [19] and the next statement can be inferred as a direct consequence.

*Theorem 4.1*
Let the unknown parameter $\vartheta$ be such that $\vartheta \in [\vartheta_i, \vartheta_{i+1}]$ for some $i = 1, ..., i_{max}$, and assume in addition that the distinguishability conditions (16)-(17) are fulfilled. Then the overall estimated state $\hat{\mathbf{x}}_t$ converges to the state $\hat{\mathbf{x}}_{t|i^\diamond}$ of the model closest to the true system $\mathbf{x}_t$ in the following sense:

$$p_t^{i^\diamond} \to 1, \quad p_t^j \to 0 \ \forall j \neq i^\diamond \tag{18}$$

where the index $i^\diamond$ is characterized by the conditions

$$\text{either } i^\diamond = i \textit{ or } i^\diamond = i+1$$

In particular, for any $\vartheta$ and any weight initial condition $\boldsymbol{\pi_0} \in \mathcal{P}$, there exists $T(\vartheta, \boldsymbol{\pi}_0) > 0$ such that the pointwise set inclusion $\hat{\vartheta}_t \in \{\vartheta_i, \vartheta_{i+1}\}$ holds true for any $t \geq T(\vartheta, \boldsymbol{\pi}_0)$.

*Proof*
The statement follows straightforwardly from Lemma 4.1, since the list of claimed values $\mathcal{T}$ does not lead to indistinguishability scenarios. In particular, thanks to (16), the terminal index $i^\diamond$ satisfies

$$i^\diamond = \arg\min_{i\in\{1,2,\ldots,i_{max}\}} \lim_{n\to\infty}\frac{1}{n}\sum_{\tau=t}^{t+n-1} s_\tau^i.$$

Now, denoting by $\Psi(\omega)$ the power spectral density of the input signals $[\mathbf{u}_t\ \mathbf{d}_t\ \boldsymbol{\mu}_t]^T$, and using the Parseval's theorem [33], it can be seen that the above condition is equivalent to

$$i^\diamond = \arg\min\{\mathcal{Y}_1, ..., \mathcal{Y}_{i_{max}}\}$$
$$\mathcal{Y}_k = tr\left[\int_{-\pi}^{\pi}(\mathbb{H}_k(e^{j\omega})\Psi(\omega)\mathbb{H}_k(e^{j\omega})^H S_{\vartheta_k}^{-1})d\omega\right]$$

where $\mathbb{H}_k(z)$ is the discrete transfer matrix of the $k^{th}$ model (see [19] for further details). Since any $\mathcal{Y}_i$ is by construction a positive and convex function of the unknown parameter and has a minimum in $\vartheta = \vartheta_k$, the estimated parameter $\hat{\vartheta}_t$ is forced to converge to one of the boundary points $\{\vartheta_i, \vartheta_{i+1}\}$ in a finite time $T(\vartheta, \boldsymbol{\pi}_0)$. □

*Remark 4.1*
Given any bounded interval $E \subset \mathbb{R}$ with $\vartheta \in E$, there exists a decomposition

$$E = E_0 \cup \bigcup_{i=1}^{i_{max}} E_i, \quad E_i = (\underline{e}_i, \overline{e}_i)$$

such that

$$\vartheta \in E_i \Rightarrow \hat{\vartheta}_t \to \vartheta_i.$$

The set $E_0$ contains all values of $\vartheta \in E$ that may lead to indistinguishability.



*Prepared using* acsauth.cls
DOI: 10.1002/acs

*Definition 4.2*
Given the threshold $\delta \in (0,1)$ and the closed subset $K = \cup_{i=1}^{i_{max}} K_i$, where $K_i \subset E_i$ are compact intervals, we define the parameter $T_{max}(K,\delta)$ as a measure of the convergence rate:

$$T_{max}(K,\delta) = \max_{\vartheta \in K} \max_{\boldsymbol{\pi}_0 \in \mathcal{P}_\delta} T(\vartheta, \boldsymbol{\pi}_0), \tag{19}$$

with

$$\mathcal{P}_\delta := \{\boldsymbol{\pi} \in \mathcal{P} : \pi_i \geq \delta \ \forall i = 1, ..., i_{max}\}.$$

The parameter $T_{max}(K,\delta)$ defined in (19) represents an upper bound for the convergence rate of the algorithm. To compute such bound one takes into account the worst case of converging time $T(\vartheta, \boldsymbol{\pi}_0)$ in terms of AWIC $\boldsymbol{\pi}_0$ and value of the parameter $\vartheta$ to be estimated. It is worth noting that the accuracy of the estimation depends on the number of multiple models being considered. As a matter of fact, many applications involve time-varying unknown quantities, and therefore a method able to adapt to possible model switchings is desirable. To this end, let us focus now on the case of a time-varying parameter

$$\vartheta = \vartheta(t).$$

Although the MMAE algorithm is designed according to a discrete-time setting, we treat $\vartheta(t)$ as a continuous-time parameter in order to emphasize the robustness of the approach with respect to uncertainties on the time-profile of $\vartheta(t)$ itself; moreover such generalized setup is well suited to handle discretized models of continuous-time systems. As a first step toward the estimation task, the update procedure (15) has to be modified in order to prevent the occurrence of the saturated scenario

$$p_t^h = 1, \ p_t^j = 0 \ \forall j \neq h \ \forall t > t_1.$$

Let us consider $\epsilon > 0$ sufficiently small, i.e. such that $\epsilon < 1/i_{max}$. For $\Delta > 0$, let us define the truncation operators

$$\begin{aligned} \mathrm{sat}_\Delta(\zeta) &= \min(\Delta, \max(\zeta, -\Delta)) \\ \mathrm{dead}_\Delta(\zeta) &= \zeta - \mathrm{sat}_\Delta(\zeta) \end{aligned}$$

Define the weights $p_i^t$ according to the following procedure:

$$\begin{cases} q_{t+1}^i = \frac{\gamma_i e^{-s_t^i}}{\sum_{j=1}^{i_{max}} p_t^j \gamma_j e^{-s_t^j}} p_t^i, \\ r_{t+1}^i = \sum_{j \neq i} \mathrm{dead}_{1-\epsilon}(q_{t+1}^j) \\ p_{t+1}^i = \mathrm{sat}_{1-\epsilon}(q_{t+1}^i) + \frac{r_{t+1}^i}{i_{max}-1} \end{cases} \tag{20}$$

The resulting dynamic weights verify $p_t^i \in [\epsilon/(i_{max}-1), 1-\epsilon] \ \forall i = 1, ..., i_{max} \ \forall t \geq 0$ and

$$\sum_{i=1}^{i_{max}} p_t^i = 1 \quad \forall t \geq 0.$$

*Assumption 4.1*
Given the admissible set $E$, assume that the indistinguishability set $E_0 \subset E$ (as introduced in Remark 4.1) is negligible, i.e.

$$|E_0| = 0.$$

*Assumption 4.2*
The unknown time-varying parameter $\vartheta(t)$ is a non-decreasing (non-increasing) Lipschitz function with constant $\mathcal{L} > 0$. Moreover it satisfies the following conditions.

a) The parameter $\vartheta(t)$ is not stationary on the indistinguishability set $E_0$, i.e.

$$|\{t \in [0,\infty) : \vartheta(t) \in E_0\}| = 0; \tag{21}$$

$$\lim_{t \to \infty} \vartheta(t) \notin E_0. \tag{22}$$




DOI: 10.1002/acs

b) A family of compact intervals $K_i \subset E_i$ with $\vartheta_i \in K_i$ can be found such that

$$\mathcal{L} < \frac{d_K}{2T_{max}(K, \epsilon_1)}, \tag{23}$$

where $d_K = \min_{i=1,...,i_{max}} |K_i|$ and $\epsilon_1 = \epsilon/(i_{max} - 1)$.

The Lipschitz condition (23) is imposed in order to guarantee that the rate of change of the unknown parameter is not larger than the rate of convergence of the estimation algorithm, so that the estimator is able to promptly adapt to the evolution of $\vartheta(t)$. In particular, under the mentioned Lipschitz assumption and using the modified weights (20), the following result can be stated, being one of the major theoretical contributions of the paper and extending the multiple-model adaptation features of Theorem 4.1 to the case of time-varying unknown parameters.

*Theorem 4.2*
*If Assumptions 4.1 and 4.2 hold true, then there exist a sequence of time intervals and a sequence of indices, namely $I_k = [\underline{\tau}_k, \overline{\tau}_k]$ and $i_k \in \{2, ..., i_{max}\}$, $k \in \mathbb{N}$, and a family of compact subintervals $J_i \subset K_i \subset E_i$ such that $\forall t \in I_k$ one has*

$$\begin{aligned}
&|I_k| \geq T_{max}(K, \epsilon_1), \\
&\vartheta(t) \in J_{i_k}, \\
&\hat{\vartheta}_t = \vartheta_{i_k}, \\
&p_t^{i_k} \to 1 - \epsilon, \quad p_t^h \to \epsilon/(i_{max} - 1) \ \forall h \neq i_k.
\end{aligned}$$

*Proof*
The proof is given in Appendix. □

The statement of the theorem may be interpreted as the existence of a family of time subintervals $J_i$ such that, on each of them, the estimated parameter $\hat{\vartheta}_t$ converges to one specific $\theta_i$, this being guaranteed by the convergence of the weight $p_t^i$ to the upper limit $1 - \epsilon$.

## 5. ICING DETECTION AND IDENTIFICATION WITH NESTED MULTIPLE MODELS

The multiple model adaptive estimator derived above will be now adapted to the aircraft system and extended to fit in a nested architecture with the aim of simultaneously estimating both the surface icing severity factor $\eta$ and the sensor icing severity factor $\xi$.
Consider the following discretized linear model derived from (5)-(6) and (8) by setting a sampling period $\tau_\varsigma > 0$ and assuming inputs and disturbances to be approximated by constant signals on each sampled interval:

$$\begin{aligned}
\mathbf{x}_{n+1} &= \bar{\mathbf{A}}_{\tau_\varsigma} \mathbf{x}_n + \bar{\mathbf{B}}_{\tau_\varsigma} \boldsymbol{\delta}_n + \bar{\mathbf{W}}_{\tau_\varsigma} \boldsymbol{\nu}_n^\dagger, \\
\mathbf{y}_n &= \mathbf{C}\mathbf{x}_n + \boldsymbol{\mu}_n
\end{aligned} \tag{24}$$

where $\bar{\mathbf{A}}_{\tau_\varsigma} = e^{\mathbf{A}\tau_\varsigma}$, $\bar{\mathbf{B}}_{\tau_\varsigma} = \int_0^{\tau_\varsigma} e^{\mathbf{A}(\tau_\varsigma - \zeta)} \mathbf{B} d\zeta$, $\bar{\mathbf{W}}_{\tau_\varsigma} = \int_0^{\tau_\varsigma} e^{\mathbf{A}(\tau_\varsigma - \zeta)} \mathbf{W} d\zeta$, and

$$\mathbf{x}_n = \mathbf{x}(n\tau_\varsigma), \quad \boldsymbol{\delta}_n = \boldsymbol{\delta}(n\tau_\varsigma), \quad \mathbf{y}_n = \mathbf{y}(n\tau_\varsigma).$$

The symbol $\boldsymbol{\nu}_n^\dagger$ indicates the average of the wind acceleration $\dot{\boldsymbol{\nu}}$ computed for $t = n\tau_\varsigma$. In addition consider a second sampling period $\sigma_\varsigma < \tau_\varsigma$ such that

$$\sigma_\varsigma = \frac{\tau_\varsigma}{n_\flat}, \quad n_\flat \leq \left[\frac{c}{d}\right], \quad n_\flat \in \mathbb{N} \tag{25}$$

where $[\cdot]$ stands for the integer part of a real number and $c, d$ are the parameters appearing in (10) and (11), i.e. the airfoil chord and the pitot tube diameter respectively. The aim is



*Prepared using* acsauth.cls
DOI: 10.1002/acs

defining two separate time scales, a faster one for estimating icing on sensors and a slower one for estimating airfoil icing: the parameters $c, d$ do characterize the two different scales indeed. This leads to the additional discretized system

$$\begin{array}{rl} \mathbf{z}_{m+1} & = \bar{\mathbf{A}}_{\sigma_\varsigma}\mathbf{z}_m + \bar{\mathbf{B}}_{\sigma_\varsigma}\boldsymbol{\upsilon}_m + \bar{\mathbf{W}}_{\sigma_\varsigma}\boldsymbol{\varpi}_m, \\ \mathbf{r}_m & = \mathbf{C}\mathbf{z}_m + \boldsymbol{\mu}_m \end{array} \tag{26}$$

where $\bar{\mathbf{A}}_{\sigma_\varsigma} = e^{\mathbf{A}_0\tau_\varsigma}$, $\bar{\mathbf{B}}_{\sigma_\varsigma} = \int_0^{\tau_\varsigma} e^{\mathbf{A}_0(\tau_\varsigma-\zeta)}\mathbf{B}_0 d\zeta$, $\bar{\mathbf{W}}_{\sigma_\varsigma} = \int_0^{\tau_\varsigma} e^{\mathbf{A}_0(\tau_\varsigma-\zeta)}\mathbf{W}_0 d\zeta$, and

$$\mathbf{z}_m = \mathbf{x}(m\sigma_\varsigma), \quad \boldsymbol{\upsilon}_m = \boldsymbol{\delta}(m\sigma_\varsigma), \quad \mathbf{r}_n = \mathbf{y}(m\sigma_\varsigma).$$

As before, $\boldsymbol{\varpi}_m^\dagger$ is the average of the wind acceleration $\dot{\boldsymbol{\nu}}$ computed over a time sample and evaluated for $t = m\sigma_\varsigma$. By construction the identity $n\tau_\varsigma = n_\flat n\sigma_\varsigma$ holds true and hence, if disturbances and inputs are nearly constant on the large period $[(n-1)\tau_\varsigma, n\tau_\varsigma]$, one has

$$\mathbf{x}_n \approx \mathbf{z}_{n_\flat n}, \quad \mathbf{y}_n \approx \mathbf{r}_{n_\flat n}.$$

Assuming the icing severity factors to be slowly-varying, the icing conditions on the system can be expressed by the following matrices with $\star \in \{\tau_\varsigma, \sigma_\varsigma\}$ :

$$\bar{\mathbf{A}}_{ice}(\star,\eta) = e^{(\mathbf{A}+\eta\mathbf{A}_\mathcal{E})\star}, \tag{27}$$

$$\bar{\mathbf{B}}_{ice}(\star,\eta) = \int_0^\star e^{(\mathbf{A}+\eta\mathbf{A}_\mathcal{E})(\star-\zeta)}(\mathbf{B}+\eta\mathbf{B}_\mathcal{E})d\zeta, \tag{28}$$

$$\bar{\mathbf{W}}_{ice}(\star,\eta) = \int_0^{\tau_\varsigma} e^{(\mathbf{A}+\eta\mathbf{A}_\mathcal{E})(\star-\zeta)}\mathbf{W} d\zeta, \tag{29}$$

$$\bar{\mathbf{F}}_{ice}(\star,\eta) = \int_0^{\tau_\varsigma} e^{(\mathbf{A}+\eta\mathbf{A}_\mathcal{E})(\star-\zeta)}\bar{\mathbf{F}} d\zeta, \tag{30}$$

$$\bar{\mathbf{C}}_{ice}(\xi) = \mathbf{C} + \xi\mathbf{C}_\mathcal{S} \tag{31}$$

Recalling that icing severity factors have been experimentally shown to be bounded [26], it is possible to select two sets of claimed parameter values $\mathcal{N} = \{\eta_1, \eta_2 ..., \eta_{i_{max}}\}$ and $\mathcal{X} = \{\xi_1, \xi_2, ..., \xi_{j_{max}}\}$ with $\eta_i < \eta_{i+1}$, $\xi_j < \xi_{j+1}$ and $\eta_1 = \xi_1 = 0$. Due to (27)-(31), one can define a bank of possible system models:

$$\begin{array}{c} \mathcal{S}_{i,j,\star} = \{\mathbf{A}_{\star,\eta_i}, \mathbf{B}_{\star,\eta_i}, \mathbf{W}_{\star,\eta_i}, \mathbf{F}_{\star,\eta_i}, \mathbf{C}_{\xi_j}\}, \\ i = 1, ..., i_{max} \quad j = 1, ..., j_{max}, \quad \star \in \{\tau_\varsigma, \sigma_\varsigma\} \end{array} \tag{32}$$

with

$$\begin{array}{l} \mathbf{A}_{\star,\eta_i} = \bar{\mathbf{A}}_{ice}(\star,\eta_i), \mathbf{B}_{\star,\eta_i} = \bar{\mathbf{B}}_{ice}(\star,\eta_i), \\ \mathbf{W}_{\star,\eta_i} = \bar{\mathbf{W}}_{ice}(\star,\eta_i)\mathbf{F}_{\star,\eta_i} = \bar{\mathbf{F}}_{ice}(\star,\eta_i), \mathbf{C}_{\xi_j} = \bar{\mathbf{C}}_{ice}(\xi_j). \end{array} \tag{33}$$

We point out that $\mathcal{S}_{1,1,\star}$ correspond to the nominal systems (24) and (26), while $\mathcal{S}_{i_{max},j_{max},\star}$ represents models of the plant with total icing conditions. In this way we can adopt a nested MMAE formulation by considering the families of minimax observers

$$\begin{array}{rl} \hat{\mathbf{x}}_{n+1|\eta_i} & = \mathbf{A}_{\tau_\varsigma,\eta_i}\hat{\mathbf{x}}_{n|\eta_i} + \mathbf{B}_{\tau_\varsigma,\eta_i}\boldsymbol{\delta}_n + \mathbf{F}_{\tau_\varsigma,\eta_i} \\ & \quad + \mathbf{D}_{\tau_\varsigma,\eta_i}(\mathbf{y}_n - \hat{\mathbf{y}}_{n|\eta_i}) \\ \hat{\mathbf{y}}_{n|\eta_i} & = \mathbf{C}_{\xi_{j^\diamond}}\hat{\mathbf{x}}_{n|\eta_i} + \xi_{j^\diamond}\bar{\mathbf{u}} \\ \mathbf{D}_{\tau_\varsigma,\eta_i} & = \mathbf{A}^T_{\tau_\varsigma,\eta_i}\boldsymbol{\Sigma}_{\eta_i}\mathbf{C}^T_{\xi_{j^\diamond}}[\mathbf{C}_{\xi_{j^\diamond}}\boldsymbol{\Sigma}_{\eta_i}\mathbf{C}^T_{\xi_{j^\diamond}} + \boldsymbol{\Omega}]^{-1}, \end{array} \tag{34}$$

and

$$\begin{array}{rl} \hat{\mathbf{z}}_{m+1|\xi_j} & = \mathbf{A}_{\sigma_\varsigma,\eta_{i^\diamond}}\hat{\mathbf{z}}_{m|\xi_j} + \mathbf{B}_{\sigma_\varsigma,\eta_{i^\diamond}}\boldsymbol{\upsilon}_m + \mathbf{F}_{\sigma_\varsigma,\eta_{i^\diamond}} \\ & \quad + \mathbf{D}_{\sigma_\varsigma,\xi_j}(\mathbf{r}_m - \hat{\mathbf{r}}_{m|\xi_j}) \\ \hat{\mathbf{r}}_{m|\xi_j} & = \mathbf{C}_{\xi_j}\hat{\mathbf{z}}_{m|\xi_j} + \xi_j\bar{\mathbf{u}} \\ \mathbf{D}_{\sigma_\varsigma,\xi_j} & = \mathbf{A}^T_{\sigma_\varsigma,\eta_{i^\diamond}}\boldsymbol{\Upsilon}_{\xi_j}\mathbf{C}^T_{\xi_j}[\mathbf{C}_{\xi_j}\boldsymbol{\Upsilon}_{\xi_j}\mathbf{C}^T_{\xi_j} + \boldsymbol{\Omega}]^{-1}, \end{array} \tag{35}$$



*Prepared using* acsauth.cls
DOI: 10.1002/acs

where the matrices $\mathbf{\Sigma}_{\eta_i}$, $\mathbf{\Upsilon}_{\xi_j}$ are the positive stabilizing solutions of the discrete algebraic Riccati equations

$$\begin{aligned} &-\mathbf{\Sigma}_{\eta_i} + \mathbf{A}^T_{\tau_\varsigma,\eta_i}\mathbf{\Sigma}_{\eta_i}\mathbf{A}_{\tau_\varsigma,\eta_i} + \mathbf{W}_{\tau_\varsigma,\eta_i}\mathbf{\Xi}\mathbf{W}^T_{\tau_\varsigma,\eta_i} \\ &-\mathbf{A}^T_{\tau_\varsigma,\eta_i}\mathbf{\Sigma}_{\eta_i}\mathbf{C}^T_{\xi_{j^\diamond}}[\mathbf{C}_{\xi_{j^\diamond}}\mathbf{\Sigma}_{\eta_i}\mathbf{C}^T_{\xi_{j^\diamond}} + \mathbf{\Omega}]^{-1}\mathbf{C}_{\xi_{j^\diamond}}\mathbf{\Sigma}_{\eta_i}\mathbf{A}_{\tau_\varsigma,\eta_i} = 0, \end{aligned} \tag{36}$$

and

$$\begin{aligned} &-\mathbf{\Upsilon}_{\xi_j} + \mathbf{A}^T_{\sigma_\varsigma,\eta_{i^\diamond}}\mathbf{\Upsilon}_{\xi_j}\mathbf{A}_{\sigma_\varsigma,\eta_{i^\diamond}} + \mathbf{W}_{\sigma_\varsigma,\eta_{i^\diamond}}\mathbf{\Xi}\mathbf{W}^T_{\sigma_\varsigma,\eta_{i^\diamond}} \\ &-\mathbf{A}^T_{\sigma_\varsigma,\eta_{i^\diamond}}\mathbf{\Upsilon}_{\xi_j}\mathbf{C}^T_{\xi_j}[\mathbf{C}_{\xi_j}\mathbf{\Upsilon}_{\xi_j}\mathbf{C}^T_{\xi_j} + \mathbf{\Omega}]^{-1}\mathbf{C}_{\xi_j}\mathbf{\Upsilon}_{\xi_j}\mathbf{A}_{\sigma_\varsigma,\eta_{i^\diamond}} = 0, \end{aligned} \tag{37}$$

with positive definite symmetric matrices $\mathbf{\Omega}, \mathbf{\Xi}$ to be computed based on the bounds on the output noise $\boldsymbol{\mu}$ and on the wind gust acceleration $\dot{\boldsymbol{\nu}}$, respectively. The last bound can be obtained based on the atmospheric conditions data and known turbulence models, e.g. Dryden model [34]. Mimicking the definitions (12)-(14), the overall estimated states $\hat{\mathbf{x}}_n$, $\hat{\mathbf{z}}_m$, estimated outputs $\hat{\mathbf{y}}_n, \hat{\mathbf{r}}_m$ and estimated icing factors $\hat{\eta}_n$, $\hat{\xi}_m$ are obtained from the MMAE as the combinations:

$$\begin{aligned} \hat{\mathbf{x}}_n &= \sum_{i=1}^{i_{max}} p^i_{\tau_\varsigma,n}\hat{\mathbf{x}}_{n|\eta_i} \qquad & \hat{\mathbf{z}}_m &= \sum_{j=1}^{j_{max}} p^j_{\sigma_\varsigma,m}\hat{\mathbf{z}}_{m|\xi_j} \\ \hat{\mathbf{y}}_n &= \sum_{i=1}^{i_{max}} p^i_{\tau_\varsigma,n}\hat{\mathbf{y}}_{n|\eta_i} \qquad & \hat{\mathbf{r}}_m &= \sum_{i=1}^{j_{max}} p^j_{\sigma_\varsigma,m}\hat{\mathbf{r}}_{m|\xi_j} \end{aligned} \tag{38}$$

$$\begin{aligned} \hat{\eta}_n &= \eta_{i^\diamond}, \quad i^\diamond := \arg \max_{i\in\{1,\dots,i_{max}\}} p^i_{\tau_\varsigma,n} \\ \hat{\xi}_m &= \xi_{j^\diamond}, \quad j^\diamond := \arg \max_{j\in\{1,\dots,j_{max}\}} p^j_{\sigma_\varsigma,m} \end{aligned} \tag{39}$$

where the dynamic weights $p^i_{\tau_\varsigma,n}$ and $p^j_{\sigma_\varsigma,m}$ are defined and updated according to (15) with

$$\mathbf{S}_{\eta_i,j^\diamond} = \mathbf{C}_{\xi_{j^\diamond}}\mathbf{\Sigma}_{\eta_i}\mathbf{C}^T_{\xi_{j^\diamond}} + \mathbf{\Omega}, \quad \mathbf{S}_{\xi_j} = \mathbf{C}_{\xi_j}\mathbf{\Upsilon}_{\xi_j}\mathbf{C}^T_{\xi_j} + \mathbf{\Omega}.$$

The basic idea of the nested multiple model approach is to exploit the two different time scales of the unknown parameters $\eta, \xi$. The mechanism, which is illustrated in the block diagram in Figure 2, can be synthesized as follows: for each iteration of the system (34) (outer loop), $n_\flat$ iterations of (35) (inner loop) are performed. We notice that, since by assumption (25) the sampling rate of the outer loop is an integer multiple of the sampling rate of the inner loop, no issue arises in the initialization nor in the synchronization of the loops.

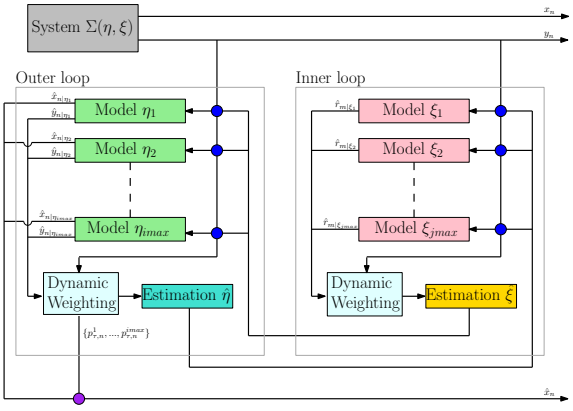


Figure 2. Block diagram of nested multiple models



DOI: 10.1002/acs

*Remark 5.1*
*We notice that, by construction, the procedure (33) yields distinct matrices for any different choice of parameters $\eta, \xi$, and therefore indistinguishability may only occur if the system output turns out to be equally distanced from two given models. However, for any fixed bank of MM, the largest set of icing values leading to such symmetry condition is a null-measure set.*

*Remark 5.2*
*The introduction of additional criterions to exclude the most unlikely events, allows us to reduce the number of models and the computational complexity. As a matter of fact, based on the temperature and humidity measurements provided by the meteorological sensor suite, a switching policy can be implemented such that the multiple-model estimation is activated if and only if certain (possibly conservative) external conditions are met, i.e. if and only if potential icing circumstances are encountered.*

The proposed nested MMAE algorithm can be stated based on (34) and (35).

**Algorithm 5.1.** $i^\diamond = j^\diamond = 1$ `% Initialization`;
`% ` $N_\sharp$ `= number of iterations`;
`For` $n = 1 : N_\sharp$
  `For` $\ell = 1 : n_\flat$
    `Run (35)`
    `Compute` $\hat{\mathbf{z}}_m,\ \hat{\mathbf{r}}_m$ `for` $m = (n-1)n_\flat + \ell$
  `End`
  `Update` $j^\diamond$
  `Run (34) and compute` $\hat{\mathbf{x}}_n,\ \hat{\mathbf{y}}_n$
  `Update` $i^\diamond$
`End`

In order to guarantee the efficiency of the previous algorithm we must require that the convergence rate of both the outer and the inner loop is sufficiently fast. In this regard the following assumptions are made, these being crucial for the establishment of the successive statement that constitutes an extension of Theorem 4.2 to the nested multiple models case with a pair of unknown parameters to be estimated. In particular, suitable bounds on the Lipschitz constants (23) that ensure the desired convergence performances can be expressed in terms of upper bounds for the growth rates (10) and (11) of the icing severity factors.

*Assumption 5.1*
The ice density $\varrho$, the liquid water content $\lambda$ and the collection efficiency $\wp$ are bounded, i.e. $\varrho \in [\varrho_{min}, \varrho_{max}]$, $\lambda \in [\lambda_{min}, \lambda_{max}]$ and $\wp \in [\wp_{min}, \wp_{max}]$.

*Assumption 5.2*
There exists a prescribed region $\hat{O} = \hat{O}_1 \times \hat{O}_2 \times \hat{O}_3 \in \mathbb{R}^9$ such that the linear systems (24) and (26) are sufficiently accurate linearized models of the aircraft dynamics (1) if $\mathbf{x} \in \hat{O}$. Accordingly we set

$$V_{max} := \max_{[u\ v\ w]^T \in \hat{O}_1} \sqrt{(u^* + u)^2 + (v^* + v)^2 + (w^* + w)^2}.$$

The region $\hat{O}$ represents the neighborhood of the trim point for which the dynamics of the aircraft is essentially linear, i.e. where higher order terms can be neglected. The next statement is the main result of this section on icing detection and identification for UAVs, and it is intended to exploit the convergence property of the proposed nested multiple-model architecture. For given compact sets $K_\tau, K_\sigma$ let us define the uniform maximal time windows

$$T^{(\tau)}_{max}(K_\sigma, \epsilon_1) := \max_{\xi \in \{\xi_1, \dots \xi_{j_{max}}\}} \{T_{max}(K_\tau, \epsilon_1) \text{ for (34)}\}$$

$$T^{(\sigma)}_{max}(K_\sigma, \epsilon_1) := \max_{\eta \in \{\eta_1, \dots \eta_{i_{max}}\}} \{T_{max}(K_\sigma, \epsilon_1) \text{ for (35)}\}$$



*Prepared using* acsauth.cls
DOI: 10.1002/acs

*Theorem 5.1*
Assume that the nested algorithm 5.1 is implemented: the multiple model estimator (35) is updated every $\sigma_\varsigma$ time units, while the multiple model estimator (34) is updated every $\tau_\varsigma = n_\flat \sigma_\varsigma$ time units. Suppose that parameters $\delta_\tau, \delta_\sigma > 0$ can be found such that, given the closed subsets $K_\tau = \cup_{i=2}^{i_{max}} [\eta_{i-1} + \delta_\tau, \eta_i - \delta_\tau]$ and $K_\sigma = \cup_{j=2}^{j_{max}} [\xi_{j-1} + \delta_\sigma, \xi_j - \delta_\sigma]$ and the maximal admissible sets $\bar{E}^{(\eta)} = [0, \eta_{max}]$ and $\bar{E}^{(\xi)} = [0, \xi_{max}]$, one has

$$f_{max} \frac{\wp_{max} \lambda_{max} V_{max}}{\varrho_{min} c} < \frac{d_{K_\tau}}{2(T^{(\sigma)}_{max}(\bar{E}^{(\xi)}, \epsilon_1) + T^{(\tau)}_{max}(K_\tau, \epsilon_1))} \tag{40}$$

$$f_{max} \frac{\wp_{max} \lambda_{max} V_{max}}{\varrho_{min} d} < \frac{d_{K_\sigma}}{2(T^{(\sigma)}_{max}(K_\sigma, \epsilon_1) + T^{(\tau)}_{max}(\bar{E}^{(\eta)}, \epsilon_1))} \tag{41}$$

Then, given the aircraft icing model

$$\begin{aligned}
\dot{\mathbf{x}}(t) &= (\mathbf{A} + \eta(t)\mathbf{A}_{\mathcal{E}})\mathbf{x}(t) + (\mathbf{B} + \eta(t)\mathbf{B}_{\mathcal{E}})\boldsymbol{\delta}(t) + \eta(t)\bar{\mathbf{F}} \\
&\quad + \mathbf{W}\dot{\boldsymbol{\nu}}(t), \\
\mathbf{y}(t) &= (\mathbf{C} + \xi(t)\mathbf{C}_{\mathcal{S}})\mathbf{x}(t) + \xi(t)\bar{\mathbf{u}} + \boldsymbol{\mu}(t), \\
\dot{\eta}(t) &= f(\omega)\frac{\wp(t)\lambda(t)\tilde{u}(t)}{\varrho(t)c}, \\
\dot{\xi}(t) &= f(\omega)\frac{\wp(t)\lambda(t)\tilde{u}(t)}{\varrho(t)d},
\end{aligned}$$

there exist two sequences of discrete intervals and two sequences of indices, namely $N_k = [\underline{n}_k, \overline{n}_k] \cap \mathbb{N}$, $M_k = [\underline{m}_k, \overline{m}_k] \cap \mathbb{N}$, $i_k \in \{2, ..., i_{max}\}$ and $j_k \in \{2, ..., j_{max}\}$, $k \in \mathbb{N}$, such that following conditions are verified:

$$\begin{aligned}
&\forall n \in N_k : \\
&\eta(n\tau_\varsigma) \in [\eta_{i_k} + \delta_\tau, \eta_{i_k+1} - \delta_\tau], \\
&\hat{\eta}_n = \eta_{i_k}, \\
&||\mathbf{y}(n\tau_\varsigma) - \hat{\mathbf{y}}_{n|\eta_{i_k}}||_{S^{-1}_{\eta_{i_k}, j^\diamond}} = \min_{i=1,...,i_{max}} ||\mathbf{y}(n\tau_\varsigma) - \hat{\mathbf{y}}_{n|\eta_i}||_{S^{-1}_{\eta_i, j^\diamond}} \\
&\forall m \in M_k : \\
&\xi(m\sigma_\varsigma) \in [\xi_{j_k} + \delta_\sigma, \xi_{j_k+1} - \delta_\sigma], \\
&\hat{\xi}_m = \xi_{j_k}, \\
&||\mathbf{y}(m\sigma_\varsigma) - \hat{\mathbf{r}}_{m|\xi_{j_k}}||_{S^{-1}_{\xi_{j_k}}} = \min_{j=1,...,j_{max}} ||\mathbf{y}(m\sigma_\varsigma) - \hat{\mathbf{r}}_{m|\xi_j}||_{S^{-1}_{\xi_j}}
\end{aligned}$$

*Proof*
The statement follows straightforwardly from Theorem 4.2 observing that, by construction, $\eta$ and $\xi$ are Lipschitz functions with

$$\mathcal{L}_\eta \leq f_{max} \frac{\wp_{max} \lambda_{max} V_{max}}{\varrho_{min} c}, \quad \mathcal{L}_\xi \leq f_{max} \frac{\wp_{max} \lambda_{max} V_{max}}{\varrho_{min} d}.$$

We notice that, since both time windows $T^{(\sigma)}_{max}(K_\sigma, \epsilon_1)$ and $T^{\tau}_{max}(K_\tau, \epsilon_1)$ appear in inequalities (40)-(41), these conditions are more restrictive than (23). However, this additional conservatism is imposed to guarantee the ability of the algorithm of handling possible transients that may arise due to the nested behavior and the presence of more than one parameter to be estimated. In particular, since the maximal time window for each loop is defined uniformly with respect to




DOI: 10.1002/acs

the other loop, in order to demonstrate the convergence of the nested multiple model estimator it is sufficient to repeat the steps of the proof of Theorem 4.2 separately for the inner and the outer estimator based on the stronger Lipschitz bounds (40)-(41). □

*Remark 5.3*
Regarding the computational burden of the proposed algorithm, one can note that the number of iterations is linear in the number of models. In particular, denoting by $\mathcal{O}_0$ the complexity of an individual estimator update, the complexity of one cycle of the outer loop turns out to be

$$(n_\flat j_{max} + i_{max})\mathcal{O}_0.$$

As a matter of fact, it is well known that Kalman-Bucy filters feature a reasonable cost-efficiency. Moreover, since the estimator matrices only depend on the claimed values, they can be computed offline prior to initialize the algorithm.

## 6. CASE STUDY: AEROSONDE UAV

In this section, the proposed nested multiple model adaptive estimation is validated through the application to the case study of a typical small unmanned aircraft, the Aerosonde UAV (AAI Corporation, Textron Inc.), which is supposed to encounter icing conditions.

Following the developments of Section II, a coupled longitudinal/lateral linearized model of the aircraft can be derived from the original nonlinear model. Such linearized model is only used to compute the bank of estimators, whose injected output is obtained from the measurement equation of the original nonlinear aircraft system. In this regard, trim values for the state and control variables have been fixed as follows:

$$u^* = 21.6\ m/s,\ v^* = 0.5\ m/s\ w^* = 2.1\ m/s$$
$$\phi^* = -0.8\ deg,\ \theta^* = 1.5\ deg,\ \psi^* = 0\ deg$$
$$p^* = 0\ rad/s,\ q^* = 0\ rad/s,\ r^* = 0\ rad/s$$
$$\delta_{th}^* = 0.48,\ \delta_e^* = 0.15,\ \delta_a^* = -0.08,\ \delta_r = -0.16.$$

The physical parameters of the UAV are given in Table 1 [23]

$$\mathbf{A} = \begin{bmatrix} -0.4491 & -0.0096 & 0.3042 & 0 & -9.7967 & 0 & 0 & -2.1672 & 0.5000 \\ -0.0175 & -0.5490 & 0.0018 & 9.7957 & 0.0036 & 0 & 2.1672 & 0 & -21.6000 \\ -0.4458 & -0.1480 & -1.9990 & 0.1371 & 0.0036 & 0 & -0.5000 & 21.6000 & 0 \\ 0 & 0 & 0 & 0 & 0 & 0 & 1.0000 & 0 & 0.0260 \\ 0 & 0 & 0 & 0 & 0 & 0 & 0 & 1.0000 & 0.0140 \\ 0 & 0 & 0 & 0 & 0 & 0 & 0 & -0.0100 & 1.0000 \\ -0.9909 & -2.6640 & -0.0994 & 0 & 0 & 0 & -8.2544 & 0 & 4.4447 \\ -0.2983 & -0.0080 & -0.5141 & 0 & 0 & 0 & 0 & -4.4333 & 0 \\ 0.1946 & 4.5642 & 0.0238 & 0 & 0 & 0.6984 & 0 & -11.1117 & \end{bmatrix}$$

$$\mathbf{B} = \begin{bmatrix} 789.7010 & -0.4378 & 0 & 0 \\ 0 & 0 & 0 & -2.0707 \\ 0 & 4.3632 & 0 & 0 \\ 0 & 0 & 0 & 0 \\ 0 & 0 & 0 & 0 \\ 0 & 0 & 0 & 0 \\ 0 & 0 & 18.0821 & 21.3524 \\ 0 & -72.4407 & 0 & 0 \\ 0 & 0 & 10.5491 & -2.4525 \end{bmatrix} \quad \mathbf{W} = \begin{bmatrix} 0.9997 & 0 & -0.0260 \\ -0.0004 & 0.9999 & -0.0140 \\ 0.0260 & 0.0140 & 0.9996 \\ 0 & 0 & 0 \\ 0 & 0 & 0 \\ 0 & 0 & 0 \\ 0 & 0 & 0 \\ 0 & 0 & 0 \\ 0 & 0 & 0 \end{bmatrix}$$



*Prepared using* acsauth.cls
DOI: 10.1002/acs

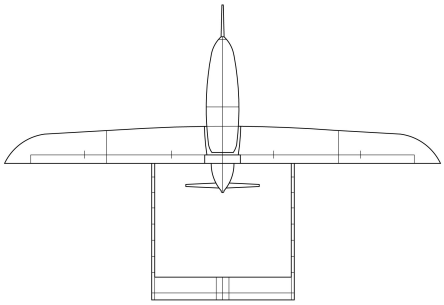

Figure 3. Aerosonde UAV

| | | | | |
|---|---|---|---|---|
| m | 13.5 Kg | | $\mathcal{S}$ | 0.55 $m^2$ |
| $J_x$ | 0.8244 $Kg/m^2$ | | $c$ | 0.1899 m |
| $J_y$ | 1.135 $Kg/m^2$ | | $b$ | 2.8956 m |
| $J_z$ | 1.759 $Kg/m^2$ | | $d$ | 3 mm |
| $J_{xz}$ | 0.1204 $Kg/m^2$ | | | |

Table 1. - Aerosonde UAV parameters

Assuming the air density $\rho = 1.2682\ Kg/m^3$, control and stability derivatives for the Aerosonde UAV are reported in [23]. The linearized system matrices $\mathbf{A}$, $\mathbf{B}$, $\mathbf{W}$ are computed accordingly and are given at the bottom of this page.
The wind force has been simulated using the standard Dryden model [34]. Typical noise levels for standard sensors on UAVs are $|\mu_\phi|, |\mu_\rho| \leq 0.01 rad$ for roll and pitch, and $|\mu_u| \leq 1 m/s$ for airspeed. On the other hand, the simulated noise and the high-frequency disturbance effects have been filtered in order to allow an easy readability of results for the incremental states $u = \tilde{u} - u^*,\ \phi = \tilde{\phi} - \phi^*$ and $\theta = \tilde{\theta} - \theta^*$ corresponding to the deviation of state variables from trim values.
Sensor inaccuracies may be handled by tuning the covariance matrices in the multiple-models design, namely $\mathbf{\Xi}$ and $\mathbf{\Omega}$; consequently, the estimator response is expected to guarantee a less tight observation error.
The icing impact coefficients $\mathcal{E}$ in the matrices $\mathbf{A}_\mathcal{E}$ and $\mathbf{B}_\mathcal{E}$ can be computed noticing that, in total icing conditions, the typical change in lift and drag coefficients has been experimentally observed to obey the following rule [26]:

- 10% reduction of coefficients $C_{Z_\alpha},\ C_{Z_{\delta_e}},\ C_{m_\alpha}, C_{m_{\delta_e}},\ C_{p_\beta},\ C_{p_p},\ C_{p_{\delta_a}}$
- 8% reduction of coefficients $C_{Y_{\delta_r}},\ C_{p_{\delta_r}},\ C_{r_r},\ C_{r_{\delta_r}}$
- 20% reduction of coefficients $C_{Y_\beta},\ C_{r_\beta}$

The nested multiple models estimation has been tested by simulating a simultaneous ice accretion on aircraft sensors and airspeed sensor according to the following evolution laws for the icing severity factors $\eta,\ \xi$:

$$\eta(t) = \begin{cases} 0 & t \leq 160 \\ linear & t \in (160, 680) \\ 0.28 & t \geq 680 \end{cases}$$

$$\xi(t) = \begin{cases} 0 & t \leq 200 \\ linear & t \in (200, 240) \\ 0.12 & t \geq 240 \end{cases}$$

The sampling periods have been fixed as $\tau_c = 0.2s$ and $\sigma_c = 0.01s$, and four different models have been considered both for the outer and the inner loop, these corresponding to the following



*Prepared using* acsauth.cls
DOI: 10.1002/acs

sets of claimed values:

$$\eta_1 = 0, \quad \eta_2 = 0.1, \quad \eta_3 = 0.2, \quad \eta_4 = 0.3$$
$$\xi_1 = 0, \quad \xi_2 = 0.1, \quad \xi_3 = 0.2, \quad \xi_4 = 0.3.$$

In this work the algebraic Riccati equations for generating the multiple-model system matrices have been solved using the `Matlab` command DARE. The control specifications are given by a closed-loop stabilizing controller, responsible to maintain the trim conditions, together with a feed-forward component defined according to an assigned constant set-point for airspeed and pitch. This choice of inputs shows that no particular maneuver is necessary to detect and identify icing, i.e. no persistency of excitation is needed. Let us stress that, in the considered practical example, Assumption IV.1 and Assumption IV.2 are satisfied: this shows indeed that, if on the one hand such technical conditions are needed to rigorously prove the theorems, on the other hand they are practically meaningful.

Figures 4(a)-(c) show the convergence of the outer estimation loop for all the three systems outputs: in particular measured airspeed, and roll and pitch angles evolve deviating from the first model and approach the forth one as the icing severity factor increases. Figure 4(d) illustrate the behavior of the estimated icing factor $\hat{\eta}$ vs the true icing factor $\eta$: it can be noticed that the estimator is affected by a very short transient while switching from model 1 to model 2: such transient is due to the occurrence of surface and sensor icing in rapid succession. In particular, as it is easily noticeable from Fig. 4(a), these have opposite effects on the airspeed, which first approaches the second model, then increases due to sensor icing occurrence, and finally starts to decrease again with a constant slope.

The convergence of the airspeed estimation in the inner loop is shown in Fig. 5(a). The other two outputs, namely roll and pitch, are not significantly affected by the sensor icing and they will not be reported. It can be noticed that, as expected, icing on the sensor produces a measured airspeed that is larger than the true airspeed. The evolution of the icing severity factor $\xi$ and its estimation $\hat{\xi}$ are depicted in Fig. 5(b).

The behavior of dynamic weights is depicted in Fig. 6(a) for the outer loop and in Fig. 6(b) for the inner loop. The transient of outer loop dynamic weights $p^1_{\tau_\varsigma}$ and $p^2_{\tau_\varsigma}$ between 200s and 400s is compatible with the aforementioned transient of estimated icing severity factor $\hat{\eta}$.

## 7. CONCLUSIONS

In this paper the problem of icing diagnosis and identification for small unmanned aerial vehicles has been tackled using a nested multiple-model framework. Referring to the coupled longitudinal/lateral model of the aircraft, which is assumed to be equipped with an airspeed sensor and inertial sensors, a bank of possible system models is defined, each one corresponding to a different claimed value of the icing severity factor. Separate effects due to icing on the aerodynamic surfaces and on the airspeed sensors have been considered, and two different estimation loops, namely outer and inner, have been designed. Such nested architecture is based on the definition of two distinct time scales for the evolution of aircraft surface icing and sensor icing, and its main advantage is reducing the computational burden and bypassing the classical issue of low scalability of multiple models. The structure of the estimators is based on the classical Krener min-max observers, and overall state and icing factor estimates are obtained as weighted combinations of the states of the models and the claimed icing values, respectively. The proposed multiple-model estimator is shown to be able to cope with changes of the unknown parameters with a very fast transient response. Numerical simulations support and validate theoretical results: the nested MMAE-based icing detection and identification scheme has been applied to the case study of the Aerosonde UAV subject to icing.

In this paper, the icing has been assumed to act uniformly on the aircraft surface, this corresponding to the so-called "total iced" conditions. The investigation of a generalized model including icing on distinct areas, for instance on the wings and on the tail, is one of the main future challenges in this research topic.




DOI: 10.1002/acs

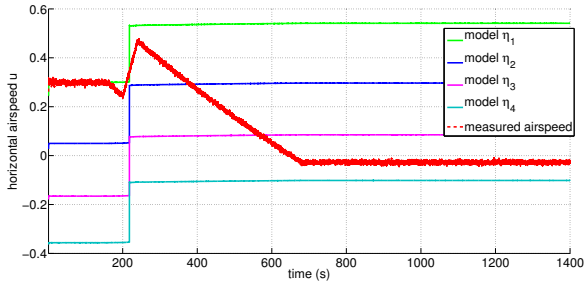


(a) Horizontal airspeed $u$

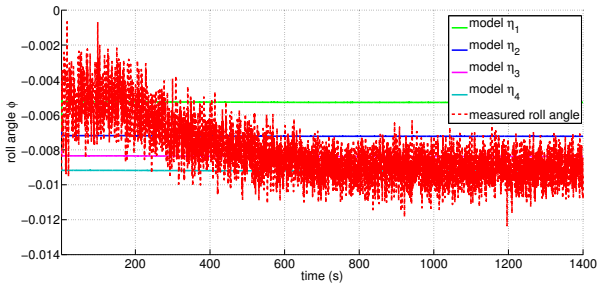


(b) Roll angle $\phi$

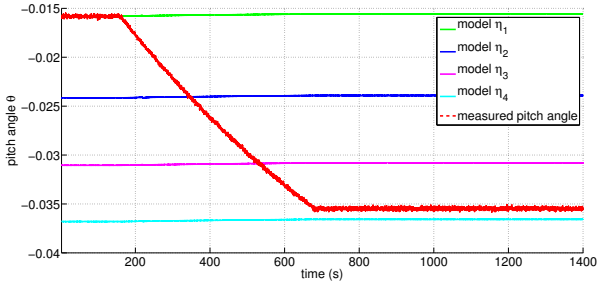


(c) Pitch angle $\theta$

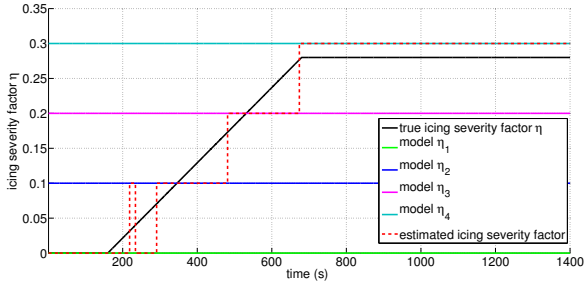


(d) Icing severity factor $\eta$

Figure 4. Nested MM Adaptive Estimation: outer loop

## ACKNOWLEDGMENTS

A. Cristofaro acknowledges funding support from ERCIM Alain Bensoussan Fellowship programme (ABCDE project - FP7 Marie Curie Actions). This work is part of the work carried out at AMOS. It is supported by the Research Council of Norway through the Centres of Excellence funding scheme, project No. 223254 - AMOS.




DOI: 10.1002/acs

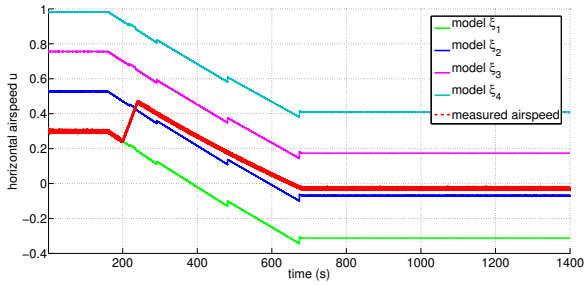


(a) Horizontal airspeed $u$

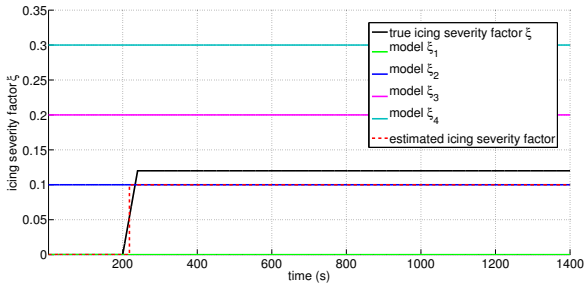


(b) Icing severity factor $\xi$

Figure 5. Nested MM Adaptive Estimation: inner loop

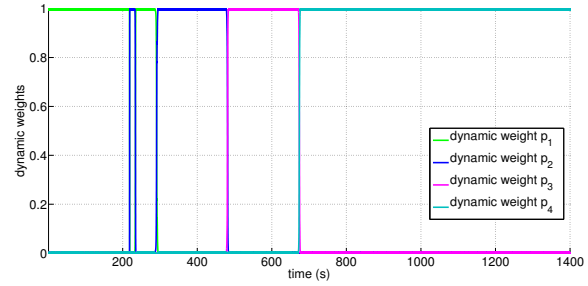


(a) Outer loop dynamic weights $p_{\tau_\varsigma}$

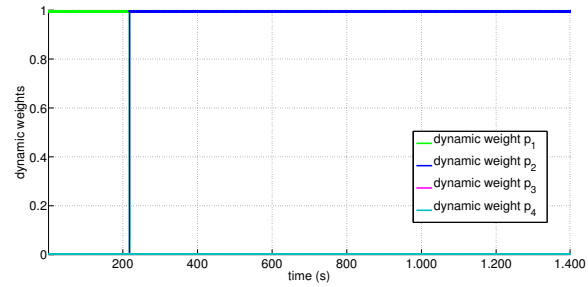


(b) Inner loop dynamic weights $p_{\sigma_\varsigma}$

Figure 6. Nested MM Adaptive Estimation: dynamic weights

## REFERENCES

1. Zhang Y, Jiang J. Bibliographical review on reconfigurable fault tolerant control systems. *Ann. Rev. in Control* 2008; **32**:229–252.



DOI: 10.1002/acs

2. Hajiyev C, Caliskan F. *Fault diagnosis and reconfiguration in flight control systems*. Springer Science & Business Media, 2003.
3. Caliskan F, Hajiyev C. A review of in-flight detection and identification of aircraft icing and reconfigurable control. *Progress in Aerospace Sciences* 2013; **60**:12–34.
4. Gent RW, Dart NP, Cansdale JT. Aircraft icing. *Phil. Trans. of the Royal Soc. of London. Series A: Mathematical, Physical and Engineering Sciences* 2000; **358**:2873–2911.
5. Myers TG, Hammond DW. Ice and water film growth from incoming supercooled droplets. *Int. Journal of Heat and Mass Transfer* 1999; **42**:2233–2242.
6. Bragg MB, Broeren AP, Blumenthal L. Iced-airfoil aerodynamics. *Progress in Aerospace Sciences* 2005; :323–362.
7. Bone S, Duff M. Carbon nanotubes to de-ice UAVs. *http://136.142.82.187/eng12/Author/data/2122.docx* Technical report, 2012; .
8. Sørensen KL, Helland AS, Johansen TA. Carbon nanomaterial-based wing temperature control system for in-flight anti-icing and de-icing of unmanned aerial vehicles. *IEEE Aerospace Conference* 2015; .
9. Miller H, Ribbens W. Detection of the loss of elevator effectiveness due to aircraft icing. *$37^{th}$ AIAA aerospace sciences meeting and exhibit, Reno* 1999; .
10. Varga A. Detection and isolation of actuator/surface faults for a large transport aircraft. *Fault Tolerant Flight Control*. Springer, 2010; 423–448.
11. Aykan R, Hajiyev C, Caliskan F. Aircraft icing detection, identification and reconfigurable control based on kalman filtering and neural networks. *AIAA Atmospheric Flight Mechanics Conference and Exhibit, San Francisco, California*, 2005.
12. Hansen S, Blanke M. Diagnosis of airspeed measurement faults for unmanned aerial vehicles. *Aerospace and Electronic Systems, IEEE Transactions on* 2014; **50**(1):224–239.
13. Ducard G, Rudin K, Omari S, Siegwart R. Strategies for sensor-fault compensation on UAVs: Review, discussions and additions. *$13^{th}$ European Control Conference*, 2014; 1963–1968.
14. Tousi M, Khorasani K. Robust observer-based fault diagnosis for an unmanned aerial vehicle. *Systems Conference (SysCon), 2011 IEEE International*, 2011; 428–434.
15. Cristofaro A, Johansen TA. An unknown input observer approach to icing detection for unmanned aerial vehicles with linearized longitudinal motion. *American Control Conference* 2015; :207–213.
16. Narendra KS, Balakrishnan J. Adaptive control using multiple models. *Automatic Control, IEEE Transactions on* 1997; **42**(2):171–187.
17. Kalkkuhl J, Johansen TA, Ludemann J. Improved transient performance of nonlinear adaptive backstepping using estimator resetting based on multiple models. *Automatic Control, IEEE Transactions on* 2002; **47**(1):136–140.
18. Hansen J, Johansen TA. Transient performance, resetting and filtering in nonlinear multiple model adaptive control. *American Control Conference*, 2004; 1223–1228.
19. Hassani V, Aguiar AP, Athans M, Pascoal AM. Multiple model adaptive estimation and model identification usign a minimum energy criterion. *American Control Conference*, 2009; 518–523.
20. Hassani V, Sorensen A, Pascoal AM, Aguiar AP. Multiple model adaptive wave filtering for dynamic positioning of marine vessels. *American Control Conference*, 2012; 6222–6228.
21. Cristofaro A, Johansen TA. Icing detection and identification for unmanned aerial vehicles: multiple model adaptive estimation. *European Control Conference* 2015; :1651–1656.
22. Seron MM, Johansen TA, Doná JAD, Cristofaro A. Detection and estimation of icing in unmanned aerial vehicles using a bank of unknown input observers. *Control Conference (AUCC), 2015 5th Australian*, 2015; 87–92.
23. Beard R, McLain T. *Small unmanned aircrafts - Theory and practice*. Princeton University press, 2012.
24. Brumbaugh RW. Aircraft model for the aiaa controls design challenge. *Journal of guidance, control, and dynamics* 1994; **17**(4):747–752.
25. Etkin B, Reid LD. *Dynamics of flight: stability and control*, vol. 3. Wiley New York, 1996.
26. Bragg MB, Hutchinson T, Merret J, Oltman R, Pokhariyal D. Effect of ice accretion on aircraft flight dynamics. *Proc. 38th AIAA Aerospace Science Meeting and Exhibit* 2000; .
27. Pokhariyal D, Bragg MB, Hutchison T, Merret J. Aircraft flight dynamics with simulated ice accretion. *AIAA Paper* 2001; **541**.
28. Myers TG. Extension to the messinger model for aircraft icing. *AIAA journal* 2001; **39**(2):211–218.
29. Krener AJ. Kalman-bucy and minimax filtering. *Automatic Control, IEEE Transactions on* 1980; **25**(2):291–292.
30. Bittanti S, Laub AJ, Willems JC. *The Riccati Equation*. Springer Science & Business Media, 2012.
31. Baram Y, Sandell Jr NR. An information theoretic approach to dynamical systems modeling and identification. *Automatic Control, IEEE Transactions on* 1978; **23**(1):61–66.
32. Baram Y, Sandell Jr NR. Consistent estimation on finite parameter sets with application to linear systems identification. *Automatic Control, IEEE Transactions on* 1978; **23**(3):451–454.
33. Haykin SS. *Adaptive filter theory*. Pearson Education India, 2008.
34. Beal T. Digital simulation of atmospheric turbulence for Dryden and Von Karman models. *Journal of guidance, control, and dynamics* 1993; **16**(1):132–138.




DOI: 10.1002/acs

## APPENDIX A

The proof of Theorem 4.2 is presented here.

The aim is to apply recursively the scheme given in Theorem 4.1. In this regard, we point out that Assumption 4.1 and Assumption 4.2 do guarantee automatically that the indistinguishability requirements of Theorem 4.1 are satisfied. Indeed, due to (21), the parameter $\vartheta(t)$ may lie in the indistinguishability set $E_0$ only for isolated time steps: without loss of generality one can therefore assume that $\vartheta(0) \notin E_0$. Three cases are admissible:

A) there exists $i_1$ such that $\vartheta(t) \in E_{i_1} \setminus K_{i_1}\ \forall t \geq 0$;
B) there exist $i_1$ and $t^{**} > 0$ such that $\vartheta(t) \in E_{i_1}\ \forall t \in [0, t^{**})$ and $\vartheta(t) \in E_{i_1+1} \setminus K_{i_1+1}\ \forall t > t^{**}$;
C) there exist $i_1$ and $t^* \geq 0$ such that $\vartheta(t) \in E_{i_1} \setminus K_{i_1}\ \forall t \in [0, t^*)$ and $\vartheta(t^*) \in K_{i_1}$.

Let us consider Case A) first. The inclusion $\vartheta(t) \in E_{i_1} \setminus K_{i_1}\ \forall t \geq t_{i_1}$, together with the non-decreasing behavior of the function $\vartheta(t)$ and condition (22), implies that there exists $\vartheta_\natural \in E_{i_1}$ with

$$\lim_{t\to\infty} \vartheta(t) = \vartheta_\natural.$$

Let $K_{i_1,\natural} \in E_{i_1}$ be an arbitrary compact set with $\vartheta(0), \vartheta_\natural \in K_{i_1,\natural}$. By construction $\vartheta(0) < \vartheta_\natural < \vartheta_{i_1}$ and hence one has

$$\max_{\boldsymbol{\pi}_0 \in \mathcal{P}_{\epsilon_1}} T(\vartheta_\natural, \boldsymbol{\pi}_0) \leq \max_{\boldsymbol{\pi}_0 \in \mathcal{P}_{\epsilon_1}} T(\vartheta(0), \boldsymbol{\pi}_0) \leq T_{max}(K_{i_1,\natural}, \epsilon_1),$$

this corresponding to

$$\vartheta(t) \in K_{i_1,\natural}, \quad \hat{\vartheta}_t = \vartheta_{i_1}\ \forall t \in I_1$$

with $I_1 = [T_{max}(K_{i_1,\natural}, \epsilon_1), \infty)$. The first case has been addressed. It is straightforward to verify that, if $\vartheta(t)$ verifies the conditions of Case B), then $\vartheta^{**}(t) := \vartheta(t + t^{**})$ is included in the previous case with $i_1$ replaced by $i_1 + 1$. In particular we can deduce

$$\vartheta(t) \in K_{i_1+1,\natural}, \quad \hat{\vartheta}_t = \vartheta_{i_1+1}\ \forall t \in I_1$$

with $I_1 = [t^{**} + T_{max}(K_{i_1+1,\natural}, \epsilon_1), \infty)$.
Let us focus now on Case C) and without loss of generality assume $t^* = 0$. Set

$$\underline{\tau}_1 = T_{max}(K, \epsilon_1).$$

By definition $\hat{\vartheta}_t$ converges to $\vartheta_{i_1}$ for, at most, $t \geq T_{max}(K_{i_1+1,\natural}, \epsilon_1)$; moreover, as long as $\vartheta(t) \in E_{i_1}$ the dynamic weights verify for $t \geq \underline{\tau}_1$

$$p_t^{i_1} \approx 1 - \epsilon, \quad p_t^h \approx \epsilon/(i_{max} - 1)\ \forall h \neq i_k.$$

Using (23), one gets

$$\vartheta(\underline{\tau}_1) - \vartheta(0) \leq \mathcal{L}\underline{\tau}_1 < \frac{d_K}{2}$$

and therefore $\vartheta(\underline{\tau}_1)$ is still included in the compact $K_{i_1}$. Define the subinterval $J_{i_1} = [\vartheta(\underline{\tau}_1), \infty) \cap K_{i_1}$ and set $\overline{\tau}_1 := \inf\{t > \underline{\tau}_1 : \vartheta(t) \in E_{i_1} \setminus K_{i_1}\}$. By construction for any $t \in I_1 = [\underline{\tau}_1, \overline{\tau}_1]$ one has $\vartheta(t) \in J_{i_1}$, and it has been shown that, on the same interval, the estimation

$$\hat{\vartheta}_t = \vartheta_{i_1}$$

holds true. Finally, if the boundary time $\overline{\tau}_1$ is finite, it can be verified that

$$|I_1| = \overline{\tau}_1 - \underline{\tau}_1 \geq \frac{\vartheta(\overline{\tau}_1) - \vartheta(\underline{\tau}_1)}{\mathcal{L}} > \frac{d_K}{2\mathcal{L}} > T_{max}(K, \epsilon_1).$$

The above procedure, i.e. the decision between cases A), B) and C), can be applied again for $t > \overline{\tau}_1$ and iterated for $k = 2, ..., i_{max}$.



*Prepared using* acsauth.cls
DOI: 10.1002/acs

## APPENDIX B

The expressions of coefficients of state and input matrix for the linearized model are reported here. First we recall that, given the principal inertia coefficients $J_x, J_y, J_z$ and $J_{xz}$ one has [23]

$$\Gamma_1 = \frac{J_{xz}(J_x - J_y + J_z)}{J_x J_z - J_{xz}^2} \quad \Gamma_2 = \frac{J_z(J_z - J_y) + J_{xz}^2}{J_x J_z - J_{xz}^2}$$
$$\Gamma_3 = \frac{J_z}{J_x J_z - J_{xz}^2} \quad \Gamma_4 = \frac{J_{xz}}{J_x J_z - J_{xz}^2} \quad \Gamma_5 = \frac{J_z - J_x}{J_y}$$
$$\Gamma_6 = \frac{J_{xz}}{J_y} \quad \Gamma_7 = \frac{J_x(J_x - J_y) + J_{xz}^2}{J_x J_z - J_{xz}^2} \quad \Gamma_8 = \frac{J_x}{J_x J_z - J_{xz}^2}$$

where $\Gamma_i$ are the inertia coefficients appearing in the expression of angular rates dynamics. Denoting by $V_a^*$ the total airspeed at the trim point, i.e. Setting

$$V_a^* := \sqrt{(u^*)^2 + (v^*)^2 + (w^*)^2}$$

and recalling that angle of attack and sideslip angle have the following expressions

$$\begin{aligned} \alpha + \alpha^* &= \alpha + \arctan \frac{w^*}{u^*} = \arctan \frac{w + w^*}{u + u^*} \\ \beta + \beta^* &= \beta + \arcsin \frac{v^*}{V_a^*} \\ &= \arcsin \frac{v + v^*}{\sqrt{(u + u^*)^2 + (v + v^*)^2 + (w + w^*)^2}} \end{aligned}$$

the linearization yields

$$\alpha = \frac{u^* w - w^* u}{(u^*)^2 + (w^*)^2},$$

$$\beta = \frac{-u^* v^* u + ((u^*)^2 + (w^*)^2)v - v^* w^* w}{(V_a^*)^2 \sqrt{((u^*)^2 + (w^*)^2)}}.$$

Moreover, setting $H_a^* := u^* u + v^* v + w^* w$ and

$$\begin{aligned} &C_X^* := C_X(\alpha^*),\ C_{X_q}^* := C_{X_q}(\alpha^*),\ C_{X_{\delta_e}}^* := C_{X_{\delta_e}}(\alpha^*) \\ &\widehat{C}_X := (C_{D_0} + C_{D_\alpha}\alpha^* + C_{L_\alpha})\sin\alpha^* \\ &\qquad +(C_{L_0} + C_{L_\alpha}\alpha^* - C_{D_\alpha})\cos\alpha^* \\ &\widehat{C}_{X_q} := C_{D_q}\sin\alpha^* + C_{L_q}\cos\alpha^* \\ &\widehat{C}_{X_{\delta_e}} := C_{D_{\delta_e}}\sin\alpha^* + C_{L_{\delta_e}}\cos\alpha^* \end{aligned}$$

$$\begin{aligned} &C_Z^* := C_Z(\alpha^*),\ C_{Z_q}^* := C_{Z_q}(\alpha^*),\ C_{Z_{\delta_e}}^* := C_{Z_{\delta_e}}(\alpha^*) \\ &\widehat{C}_Z := -(C_{D_0} + C_{D_\alpha}\alpha^* + C_{L_\alpha})\cos\alpha^* \\ &\qquad +(C_{L_0} + C_{L_\alpha}\alpha^* - C_{D_\alpha})\sin\alpha^* \\ &\widehat{C}_{Z_q} := -C_{D_q}\cos\alpha^* + C_{L_q}\sin\alpha^* \\ &\widehat{C}_{Z_{\delta_e}} := -C_{D_{\delta_e}}\cos\alpha^* + C_{L_{\delta_e}}\sin\alpha^* \end{aligned}$$

the formulae of coefficients appearing in the plant matrices $\mathbf{A}$, $\mathbf{B}$ of the linear model (5) can be computed, and are reported in Tables 2-4.



*Prepared using* acsauth.cls
DOI: 10.1002/acs

| | |
|---|---|
| $X_u$ | $\frac{\rho u^* S}{m}\left(C_X^* + C_{X_q}^* \frac{cq^*}{2V_a^*} + C_{X_{\delta_e}}^* \delta_e^*\right) - \frac{\rho (V_a^*)^2 S}{2m}\left(\left(\widehat{C}_X + \widehat{C}_{X_q} \frac{cq^*}{2V_a^*} + \widehat{C}_{X_{\delta_e}} \delta_e^*\right) \frac{w^*}{(u^*)^2 + (w^*)^2} + \frac{cq^* u^*}{2(V_a^*)^3} C_{X_q}^*\right) - \frac{\rho K u^*}{m}$ |
| $X_v$ | $r^* + \frac{\rho v^* S}{m}\left(C_X^* + C_{X_q}^* \frac{cq^*}{2V_a^*} + C_{X_{\delta_e}}^* \delta_e^*\right) - \frac{\rho S c q^* v^*}{4mV_a^*} C_{X_q}^* - \frac{\rho K v^*}{m}$ |
| $X_w$ | $-q^* + \frac{\rho w^* S}{m}\left(C_X^* + C_{X_q}^* \frac{cq^*}{2V_a^*} + C_{X_{\delta_e}}^* \delta_e^*\right) + \frac{\rho (V_a^*)^2 S}{2m}\left(\left(\widehat{C}_X + \widehat{C}_{X_q} \frac{cq^*}{2V_a^*} + \widehat{C}_{X_{\delta_e}} \delta_e^*\right) \frac{u^*}{(u^*)^2 + (w^*)^2} - \frac{cq^* w^*}{2(V_a^*)^3} C_{X_q}^*\right) - \frac{\rho K w^*}{m}$ |
| $X_\theta$ | $-g\cos\theta^*$ |
| $X_q$ | $-w^* + \frac{\rho V_a^* S c}{4m} C_{X_q}^*$ |
| $X_r$ | $v^*$ |
| $Y_u$ | $-r^* + \frac{\rho u^* S}{m}\left(C_{Y_0} + C_{Y_\beta}\beta^* + C_{Y_p}\frac{bp^*}{2V_a^*} + C_{Y_r}\frac{br^*}{2V_a^*} + C_{Y_{\delta_a}}\delta_a^* + C_{Y_{\delta_r}}\delta_r^*\right) - \frac{\rho u^* v^* S C_{Y_\beta}}{2m\sqrt{(u^*)^2 + (w^*)^2}} - \frac{\rho S b u^* (C_{Y_p} p^* + C_{Y_r} r^*)}{4mV_a^*}$ |
| $Y_v$ | $\frac{\rho v^* S}{m}\left(C_{Y_0} + C_{Y_\beta}\beta^* + C_{Y_p}\frac{bp^*}{2V_a^*} + C_{Y_r}\frac{br^*}{2V_a^*} + C_{Y_{\delta_a}}\delta_a^* + C_{Y_{\delta_r}}\delta_r^*\right) + \frac{\rho((u^*)^2 + (w^*)^2) S C_{Y_\beta}}{2m} - \frac{\rho S b v^* (C_{Y_p} p^* + C_{Y_r} r^*)}{4mV_a^*}$ |
| $Y_w$ | $p + \frac{\rho w^* S}{m}\left(C_{Y_0} + C_{Y_\beta}\beta^* + C_{Y_p}\frac{bp^*}{2V_a^*} + C_{Y_r}\frac{br^*}{2V_a^*} + C_{Y_{\delta_a}}\delta_a^* + C_{Y_{\delta_r}}\delta_r^*\right) - \frac{\rho v^* w^* S C_{Y_\beta}}{2m\sqrt{(u^*)^2 + (w^*)^2}} - \frac{\rho S b w^* (C_{Y_p} p^* + C_{Y_r} r^*)}{4mV_a^*}$ |
| $Y_\phi$ | $g\cos(\theta^*)\cos(\phi^*)$ |
| $Y_\theta$ | $-g\sin(\theta^*)\sin(\phi^*)$ |
| $Y_p$ | $w^* + \frac{\rho V_a^* S b}{4m} C_{Y_p}$ |
| $Y_r$ | $-u^* + \frac{\rho V_a^* S b}{4m} C_{Y_r}$ |
| $Z_u$ | $q^* + \frac{\rho u^* S}{m}\left(C_Z^* + C_{Z_q}^* \frac{cq^*}{2V_a^*} + C_{Z_{\delta_e}}^* \delta_e^*\right) + \frac{\rho (V_a^*)^2 S}{2m}\left(-\left(\widehat{C}_Z + \widehat{C}_{Z_q} \frac{cq^*}{2V_a^*} + \widehat{C}_{Z_{\delta_e}} \delta_e^*\right) \frac{w^*}{(u^*)^2 + (w^*)^2} - \frac{cq^* u^*}{2(V_a^*)^3} C_{Z_q}^*\right)$ |
| $Z_v$ | $-p^* + \frac{\rho v^* S}{m}\left(C_Z^* + C_{Z_q}^* \frac{cq^*}{2V_a^*} + C_{Z_{\delta_e}}^* \delta_e^*\right) - \frac{\rho S c q^* v^*}{4mV_a^*} C_{Z_q}^*$ |
| $Z_w$ | $\frac{\rho w^* S}{m}\left(C_Z^* + C_{Z_q}^* \frac{cq^*}{2V_a^*} + C_{Z_{\delta_e}}^* \delta_e^*\right) + \frac{\rho (V_a^*)^2 S}{2m}\left(\left(\widehat{C}_Z + \widehat{C}_{Z_q} \frac{cq^*}{2V_a^*} + \widehat{C}_{Z_{\delta_e}} \delta_e^*\right) \frac{u^*}{(u^*)^2 + (w^*)^2} - \frac{cq^* w^*}{2(V_a^*)^3} C_{Z_q}^*\right)$ |
| $Z_\phi$ | $-g\cos(\theta^*)\sin(\phi^*)$ |
| $Z_\theta$ | $-g\sin(\theta^*)\sin(\phi^*)$ |
| $Z_p$ | $-v^*$ |
| $Z_q$ | $u^* + \frac{\rho V_a^* S c}{4m} C_{Z_q}^*$ |

Table 2. - State matrix coefficients: velocities

| | | | | |
|---|---|---|---|---|
| $\Phi_\phi$ | $q^*\cos(\phi^*)\tan(\theta^*) - r^*\sin(\phi^*)\tan(\theta^*)$ | | $X_{\delta_t}$ | $\frac{\rho K_\chi{}^2 \delta_t^*}{m}$ |
| $\Phi_\theta$ | $\frac{q^*\sin\phi^*}{\cos^2\theta^*} + \frac{r^*\cos\phi^*}{\cos^2\theta^*}$ | | $X_{\delta_e}$ | $C_{X_{\delta_e}}^* \frac{\rho (V_a^*)^2 S}{2m}$ |
| $\Phi_p$ | $1$ | | $Y_{\delta_a}$ | $C_{Y_{\delta_a}} \frac{\rho (V_a^*)^2 S}{2m}$ |
| $\Phi_q$ | $\sin\phi^*\tan\theta^*$ | | $Y_{\delta_r}$ | $C_{Y_{\delta_r}} \frac{\rho (V_a^*)^2 S}{2m}$ |
| $\Phi_r$ | $\cos\phi^*\tan\theta^*$ | | $Z_{\delta_e}$ | $C_{Z_{\delta_e}}^* \frac{\rho (V_a^*)^2 S}{2m}$ |
| $\Theta_\phi$ | $-q^*\sin\phi^* - r^*\cos\phi^*$ | | $L_{\delta_a}$ | $(\Gamma_3 C_{p_{\delta_a}} + \Gamma_4 C_{r_{\delta_a}}) \frac{\rho (V_a^*)^2 S b}{2}$ |
| $\Theta_q$ | $\cos\phi^*$ | | $L_{\delta_r}$ | $(\Gamma_3 C_{p_{\delta_r}} + \Gamma_4 C_{r_{\delta_r}}) \frac{\rho (V_a^*)^2 S b}{2}$ |
| $\Theta_r$ | $-\sin\phi^*$ | | $M_{\delta_e}$ | $C_{m_{\delta_e}} \frac{\rho (V_a^*)^2 S c}{2J_y}$ |
| $\Psi_\phi$ | $q^*\cos(\phi^*)\sec(\theta^*) - r^*\sin(\phi^*)\sec(\theta^*)$ | | $N_{\delta_a}$ | $(\Gamma_4 C_{p_{\delta_a}} + \Gamma_8 C_{r_{\delta_a}}) \frac{\rho (V_a^*)^2 S b}{2}$ |
| $\Psi_\theta$ | $\frac{q^*\sin(\phi^*)\sin(\theta^*)}{\cos^2\theta^*} + \frac{r^*\cos(\phi^*)\sin(\theta^*)}{\cos^2\theta^*}$ | | $N_{\delta_r}$ | $(\Gamma_4 C_{p_{\delta_r}} + \Gamma_8 C_{r_{\delta_r}}) \frac{\rho (V_a^*)^2 S b}{2}$ |
| $\Psi_q$ | $\sin(\phi^*)\sec(\theta^*)$ | | | |
| $\Psi_r$ | $\cos(\phi^*)\sec(\theta^*)$ | | | |

Table 3. - Euler angles coefficients and input matrix coefficients



DOI: 10.1002/acs

| | |
|---|---|
| $P_u$ | $\rho u^* Sb\left(C_{p_0}+C_{p_\beta}\beta^*+C_{p_p}\frac{bp^*}{2V_a^*}+C_{p_r}\frac{br^*}{2V_a^*}+C_{p_{\delta_a}}\delta_a^*+C_{p_{\delta_r}}\delta_r^*\right)-\frac{\rho(V_a^*)^2Sb}{2}\left(\frac{C_{p_p}u^*p^*+C_{p_r}u^*r^*}{2(V_a^*)^3}+\frac{u^*v^*SC_{p_\beta}}{2m(V_a^*)^2\sqrt{(u^*)^2+(w^*)^2}}\right)$ |
| $P_v$ | $\rho v^* Sb\left(C_{p_0}+C_{p_\beta}\beta^*+C_{p_p}\frac{bp^*}{2V_a^*}+C_{p_r}\frac{br^*}{2V_a^*}+C_{p_{\delta_a}}\delta_a^*+C_{p_{\delta_r}}\delta_r^*\right)-\frac{\rho(V_a^*)^2Sb}{2}\left(\frac{C_{p_p}v^*p^*+C_{p_r}v^*r^*}{2(V_a^*)^3}-\frac{((u^*)^2+(w^*)^2)SC_{p_\beta}}{2m(V_a^*)^2}\right)$ |
| $P_w$ | $\rho w^* Sb\left(C_{p_0}+C_{p_\beta}\beta^*+C_{p_p}\frac{bp^*}{2V_a^*}+C_{p_r}\frac{br^*}{2V_a^*}+C_{p_{\delta_a}}\delta_a^*+C_{p_{\delta_r}}\delta_r^*\right)-\frac{\rho(V_a^*)^2Sb}{2}\left(\frac{C_{p_p}w^*p^*+C_{p_r}w^*r^*}{2(V_a^*)^3}+\frac{v^*w^*SC_{p_\beta}}{2m(V_a^*)^2\sqrt{(u^*)^2+(w^*)^2}}\right)$ |
| $L_u$ | $\Gamma_3P_u+\Gamma_4R_u$ |
| $L_v$ | $\Gamma_3P_v+\Gamma_4R_v$ |
| $L_w$ | $\Gamma_3P_w+\Gamma_4R_w$ |
| $L_p$ | $\Gamma_1q^*+(\Gamma_3C_{p_p}+\Gamma_4C_{r_p})\frac{\rho V_a^*Sb^2}{4}$ |
| $L_q$ | $\Gamma_1p^*-\Gamma_2r^*$ |
| $L_r$ | $-\Gamma_2q^*+(\Gamma_3C_{p_r}+\Gamma_4C_{r_r})\frac{\rho V_a^*Sb^2}{4}$ |
| $M_u$ | $\frac{\rho u^*Sc}{J_y}\left(C_{m_0}+C_{m_\alpha}\alpha^*+C_{m_q}\frac{cq^*}{2V_a^*}+C_{m_{\delta_e}}\delta_e^*\right)-\frac{\rho(V_a^*)^2Sc}{2J_y}\left(C_{m_\alpha}\frac{w^*}{(u^*)^2+(w^*)^2}+C_{m_q}\frac{cq^*u^*}{2(V_a^*)^3}\right)$ |
| $M_v$ | $\frac{\rho v^*Sc}{J_y}\left(C_{m_0}+C_{m_\alpha}\alpha^*+C_{m_q}\frac{cq^*}{2V_a^*}+C_{m_{\delta_e}}\delta_e^*\right)-C_{m_q}\frac{\rho Sc^2q^*v^*}{4J_yV_a^*}$ |
| $M_w$ | $\frac{\rho w^*Sc}{J_y}\left(C_{m_0}+C_{m_\alpha}\alpha^*+C_{m_q}\frac{cq^*}{2V_a^*}+C_{m_{\delta_e}}\delta_e^*\right)-\frac{\rho(V_a^*)^2Sc}{2J_y}\left(C_{m_\alpha}\frac{-u^*}{(u^*)^2+(w^*)^2}+C_{m_q}\frac{cq^*w^*}{2(V_a^*)^3}\right)$ |
| $M_p$ | $\Gamma_5r^*-2\Gamma_6p^*$ |
| $M_q$ | $C_{m_q}\frac{\rho V_a^*Sc^2}{4J_y}$ |
| $M_r$ | $\Gamma_5p^*+2\Gamma_6r^*$ |
| $R_u$ | $\rho u^* Sb\left(C_{r_0}+C_{r_\beta}\beta^*+C_{r_p}\frac{bp^*}{2V_a^*}+C_{r_r}\frac{br^*}{2V_a^*}+C_{r_{\delta_a}}\delta_a^*+C_{r_{\delta_r}}\delta_r^*\right)-\frac{\rho(V_a^*)^2Sb}{2}\left(\frac{C_{r_p}u^*p^*+C_{r_r}u^*r^*}{2(V_a^*)^3}+\frac{u^*v^*SC_{r_\beta}}{2m(V_a^*)^3\sqrt{(u^*)^2+(w^*)^2}}\right)$ |
| $R_v$ | $\rho v^* Sb\left(C_{r_0}+C_{p_\beta}\beta^*+C_{r_p}\frac{bp^*}{2V_a^*}+C_{r_r}\frac{br^*}{2V_a^*}+C_{r_{\delta_a}}\delta_a^*+C_{r_{\delta_r}}\delta_r^*\right)-\frac{\rho(V_a^*)^2Sb}{2}\left(\frac{C_{r_p}v^*p^*+C_{r_r}v^*r^*}{2(V_a^*)^3}-\frac{((u^*)^2+(w^*)^2)SC_{r_\beta}}{2m(V_a^*)^2}\right)$ |
| $R_w$ | $\rho w^* Sb\left(C_{r_0}+C_{r_\beta}\beta^*+C_{r_p}\frac{bp^*}{2V_a^*}+C_{r_r}\frac{br^*}{2V_a^*}+C_{r_{\delta_a}}\delta_a^*+C_{r_{\delta_r}}\delta_r^*\right)-\frac{\rho(V_a^*)^2Sb}{2}\left(\frac{C_{r_p}w^*p^*+C_{r_r}w^*r^*}{2(V_a^*)^3}+\frac{v^*w^*SC_{r_\beta}}{2m(V_a^*)^3\sqrt{(u^*)^2+(w^*)^2}}\right)$ |
| $R_u$ | $\Gamma_4P_u+\Gamma_8R_u$ |
| $R_v$ | $\Gamma_4P_v+\Gamma_8R_v$ |
| $R_w$ | $\Gamma_4P_w+\Gamma_8R_w$ |
| $N_p$ | $\Gamma_7q^*+(\Gamma_4C_{p_p}+\Gamma_8C_{r_p})\frac{\rho V_a^*Sb^2}{4}$ |
| $N_q$ | $\Gamma_7p^*-\Gamma_1r^*$ |
| $N_r$ | $-\Gamma_1q^*+(\Gamma_4C_{p_r}+\Gamma_8C_{r_r})\frac{\rho V_a^*Sb^2}{4}$ |

Table 4. - State matrix coefficients: angular rates



DOI: 10.1002/acs